TURUN YLIOPISTON JULKAISUJA
ANNALES UNIVERSITATIS TURKUENSIS

SARJA - SER. A I OSA - TOM. 387

ASTRONOMICA - CHEMICA - PHYSICA - MATHEMATICA

Studies of Eu- and Yb-induced Reconstructions on the Si(100) Surface

by

Riitta Perälä

TURUN YLIOPISTO
Turku 2008

From the Department of Physics and Astronomy
University of Turku
Turku, Finland

Supervised by

Professor Juhani Väyrynen
Department of Physics and Astronomy
University of Turku
Turku, Finland

Reviewed by

Docent Jouko Lahtinen
Laboratory of Physics
Helsinki University of Technology
Helsinki, Finland

and

Dr. Ergo Nõmmiste
Institute of Physics
University of Tartu
Tartu, Estonia

ISBN 978-951-29-3774-5 (PRINT)
ISBN 978-951-29-3775-2 (PDF)
ISSN 0082-7002
Painosalama Oy – Turku, Finland 2008

Contents

Acknowledgements

I would like to express my gratitude to my supervisor, Professor Juhani Väyrynen, who first introduced me to the subject of surface science and has provided his support and the excellent conditions to carry out this work ever since.

I am grateful to Dr. Mikhail Kuzmin for introducing me to the fruitful research area of rare earth metals on semiconductor surfaces. His cooperation during visits to Turku and our beamtimes in MAX-lab have formed the basis to this work. In addition, he has provided 'on-line' discussion services whenever I have needed them.

Professor Edwin Kukk is acknowledged for arranging periods of financial support. Docent Jouko Lahtinen and Dr Ergo Nõmmiste are acknowledged for their valuable comments upon reviewing this thesis. Dr Milla Kibble is thanked for reviewing the language in the thesis.

The present and former colleagues in the Materials Physics and Materials Science groups are acknowledged for their cooperation. I would especially like to mention Tapio Ollonqvist, who first introduced me to the synchrotron radiation; Hannu Ollila, who maintained our experimental set-up in the best possible condition and solved our technical problems, even the non-scientific ones; Teemu Laine, Mika Kivitörmä, Riikka-Liisa Vaara, Sari Mattila, Taina Laiho, Robert Socha, Pekka Laukkanen, and Marja Ahola-Tuomi, who have been inspiring colleagues as well as friends outside the laboratory. All of the ladies who participated in the activities arranged by 'The Materials Science Girls' are acknowledges for joyful times.

The MAX-lab staff are acknowledged for the excellent organization of our visits and for the pleasant working environment. Special thanks go to the beam line manager of BL33, Dr. T. Balasubramanian.

The Personnel in the Department of Physics and Astronomy are thanked for their cooperation.

Financial support from the EC Transnational Access to Research Infrastructures project (within the IA-SFS program) and the Academy of Finland are acknowledged.

Turku, November 2008
Riitta Perälä
Riitta Perälä

Abstract

This thesis presents experimental studies of rare earth (RE) metal induced structures on Si(100) surfaces. Two divalent RE metal adsorbates, Eu and Yb, are investigated on nominally flat Si(100) and on vicinal, stepped Si(100) substrates. Several experimental methods have been applied, including scanning tunneling microscopy/spectroscopy (STM/STS), low energy electron diffraction (LEED), synchrotron radiation photoelectron spectroscopy (SR-PES), Auger electron spectroscopy (AES), thermal desorption spectroscopy (TDS), and work function change measurements ($\Delta\varphi$).

Two stages can be distinguished in the initial growth of the RE/Si interface: the formation of a two-dimensional (2D) adsorbed layer at submonolayer coverage and the growth of a three-dimensional (3D) silicide phase at higher coverage. The 2D phase is studied for both adsorbates in order to discover whether they produce common reconstructions or reconstructions common to the other RE metals. For studies of the 3D phase Yb is chosen due to its ability to crystallize in a hexagonal AlB_2 type lattice, which is the structure of RE silicide nanowires, therefore allowing for the possibility of the growth of one-dimensional (1D) wires.

It is found that despite their similar electronic configuration, Eu and Yb do not form similar 2D reconstructions on Si(100). Instead, a wealth of 2D structures is observed and atomic models are proposed for the 2×3-type reconstructions. In addition, adsorbate induced modifications on surface morphology and orientational symmetry are observed. The formation of the Yb silicide phase follows the Stranski-Krastanov growth mode. Nanowires with the hexagonal lattice are observed on the flat Si(100) substrate, and moreover, an unexpectedly large variety of growth directions are revealed. On the vicinal substrate the growth of the silicide phase as 3D islands and wires depends drastically on the growth conditions. The conditions under which wires with high aspect ratio and single orientation parallel to the step edges can be formed are demonstrated.

List of papers

This thesis consists of the seven papers listed below. I have participated in the experimental work and contributed to the interpretation of results for all of the papers. I have been the main author for papers II and VII and co-author for the other papers.

I *Initial stages of Yb/Si(100) interface growth: 2×3 and 2×6 reconstructions*, M. Kuzmin, R. E. Perälä, P. Laukkanen, R.-L. Vaara, M. A. Mittsev, I. J. Väyrynen, Appl. Surf. Sci. 214, 196 (2003).

II *Eu- and Yb-induced reconstructions on a vicinal Si(100) surface*, R. E. Perälä, M. Kuzmin, P. Laukkanen, R.-L. Vaara, I. J. Väyrynen, Surf. Sci. 584, 8 (2005).

III *Observation of double- to single-domain transition on the Eu/Si(100) surface by LEED and STM*, M. Kuzmin, P. Laukkanen, R. E. Perälä, R.-L. Vaara, I. J. Väyrynen, Surf. Sci. 584, 1 (2005).

IV *Atomic geometry and electronic structure of the Si(100)2×3-Eu surface phase*, M. Kuzmin, R. E. Perälä, P. Laukkanen, I. J. Väyrynen, Phys. Rev. B 72, 085343 (2005).

V *Formation of ytterbium silicide film on Si(001) by solid-phase epitaxy*, M. Kuzmin, R. E. Perälä, R.-L. Vaara, P. Laukkanen, I. J. Väyrynen, J. Cryst. Growth 262, 231 (2004).

VI *Formation of ytterbium nanowires on Si(001)*, M. Kuzmin, P. Laukkanen, R. E. Perälä, R.-L. Vaara, I. J. Väyrynen, Appl. Surf. Sci. 222, 394 (2004).

VII *Ytterbium on vicinal Si(100): Growth and properties of the 2D wetting layer and the Yb silicide phase*, R. E. Perälä, M. Kuzmin, P. Laukkanen, M. Ahola-Tuomi, M. P. J. Punkkinen, I. J. Väyrynen, accepted to Surf. Sci. (2008), doi: 10.1016/j.susc.2008.10.026

The following papers, to which I have contributed, are related to this work but not included in the thesis:

VIII *Yb, Eu, and (Yb + Eu)-stabilized 3 × 1 and 3 × 2 reconstructions on Si(1 1 1)*, M. Kuzmin, R. -L. Vaara, P. Laukkanen, R. E. Perälä and I. J. Väyrynen, Sur. Sci. 538, 124 (2003)

IX *Formation and thermal-desorption-controlled patterning of Yb-induced structures on vicinal Si(1 1 1) $[\bar{1}\,\bar{1}\,2]$-miscut surface*, R. -L. Vaara, M. Kuzmin, R. E. Perälä, P. Laukkanen and I. J. Väyrynen, Surf. Sci. 529, L229 (2003)

X *Two series of triple- and single-domain reconstructions induced by europium on vicinal Si(1 1 1) $[\bar{1}\,\bar{1}\,2]$-miscut surface*, R. -L. Vaara, M. Kuzmin, P. Laukkanen, R. E. Perälä and I. J. Väyrynen, Appl. Surf. Sci. 220, 327 (2003)

XI *Evolution of step and terrace structure on $[\bar{1}\,\bar{1}\,2]$- and $[11\bar{2}]$ -miscut Si(1 1 1) surfaces upon formation of triple- and single-domain Yb-induced 3 × 2 reconstruction*, R. -L. Vaara, M. Kuzmin, R. E. Perälä, P. Laukkanen and I. J. Väyrynen, Surf. Sci. 539, 72 (2003)

XII *Structural and statistical analysis of Yb/Si(1 1 1) and Eu/Si(1 1 1) reconstructions*, M. Kuzmin, R. -L. Vaara, P. Laukkanen, R. E. Perälä and I. J. Väyrynen, Surf. Sci. 549, 183 (2004)

XIII *Atomic structure of the Eu/Si(111) 3×2 , 5×1 , and 7×1 surfaces studied by photoelectron spectroscopy,* M. Kuzmin, P. Laukkanen, R. E. Perälä, R.-L. Vaara, and I. J. Väyrynen, Phys. Rev. B 71, 155334 (2005)

XIV *High-resolution core-level photoemission study of Eu-induced (3×2)/(3×4) reconstruction on Ge(111)*, M. Kuzmin, R. E. Perälä, P. Laukkanen, M. Ahola-Tuomi, and I. J. Väyrynen, Phys. Rev. B 74, 115320 (2006)

XV *Scanning tunneling microscopy study of the Eu-induced Ge(111)-(3×2)/(3×4) reconstruction*, M. Kuzmin, P. Laukkanen, R. E. Perälä, and I. J. Väyrynen, Phys. Rev. B 73, 125332 (2006)

XVI *Atomic and electronic structure of the Yb/Ge(111)-(3×2) surface studied by high-resolution photoelectron spectroscopy*, M. Kuzmin, K. Schulte, P. Laukkanen, M. Ahola-Tuomi, R. E. Perälä, M. Adell, T. Balasubramanian, and I. J. Väyrynen, Phys. Rev. B 75, 165305 (2007)

XVII *Yb-induced (2×3) and (2×4) reconstructions on Si(100) studied by first-principles calculations and high-resolution core-level photoelectron spectroscopy*, M. Kuzmin, M. P. J. Punkkinen, P. Laukkanen, R. E. Perälä, M. Ahola-Tuomi, T. Balasubramanian, I. J. Väyrynen, Phys. Rev. B 78, 045318 (2008)

1. Introduction

Most physical properties of a surface depend on the specific atomic structure of the surface, and can be largely different from those of a given bulk solid. The creation of a semiconductor surface creates dangling bonds with charge densities that are energetically unfavourable; therefore, the surface reconstructs to minimize its energy. The main principles of surface reconstruction for elemental semiconductors are as follows: (i) the surface rearranges to reduce the amount of surface dangling bonds, (ii) the surface rearranges to produce a semiconducting surface by opening a gap between the highest occupied and lowest unoccupied surface states, and (iii) the surface structure is the lowest energy structure kinetically obtainable under the given preparation conditions. A constraint on the surface relaxations is that there is a limited amount of local surface and subsurface strain that can be accommodated. The surface reconstruction is determined by the balance between the energy gain due to the reduction of the dangling bonds and the energy cost due to induced strain.

The most intensively studied semiconductor surface has been Si(100) due to its major role in the electronic device industry. As a result, the atomic and electronic properties of the Si(100) surface are documented in detail. The conventional lithographic fabrication methods of the microelectronics industry are about to come to their fundamental limits in the effort to produce ever-smaller devices. Alternative techniques to create structures in nanometer scale are based on self-organized growth and self-assembly on atomically well-defined surfaces.

Epitaxial growth is one of the most important techniques used to fabricate various electronic and optical devices, as well as nanostructures such as quantum wires and quantum dots, because it gives highly perfect structures with high density. However, the common problem is that such nanostructures are randomly placed on substrates. Rare earth (RE) metal silicides have attracted interest in the academic community and in industry as they can have applications, for example, in integrated electronic circuits. The RE silicides have characteristic properties, like the lowest known Schottky barrier height on n-type Si, a low temperature of formation, a good electrical and thermal conductivity, and moreover, they can be grown epitaxially on Si(100).

In this thesis the growth of the two divalent RE metals, Eu and Yb, on Si(100) have been investigated. Several experimental techniques have been applied to study the RE/Si interface formation. As a substrate, two types of single crystal Si(100) surface were used: nominally flat and vicinal. The coverage range of the RE metal varied from submonolayer regime up to 20 monolayers. Two different phases can be distinguished in the growth process: a two-dimensional wetting layer with ordered reconstructions and a three-dimensional silicide phase. The aim of this study was to investigate the formation and properties of both of the above phases.

2. The Si(100) surface

Silicon crystallizes into a diamond lattice, which is built out of two interpenetrating fcc sublattices, as shown in Fig. 2.1. The bulk lattice constant a_0 for Si is 5.43 Å and the surface lattice constant a on the (100) surface is 3.84 Å. In the diamond lattice, each atom is tetrahedrally bonded to its nearest neighbours. In the case of Si, the bonds have a purely covalent character. It can be expected that the surface of a bulk solid with covalent bonds reconstructs significantly and is chemically active.

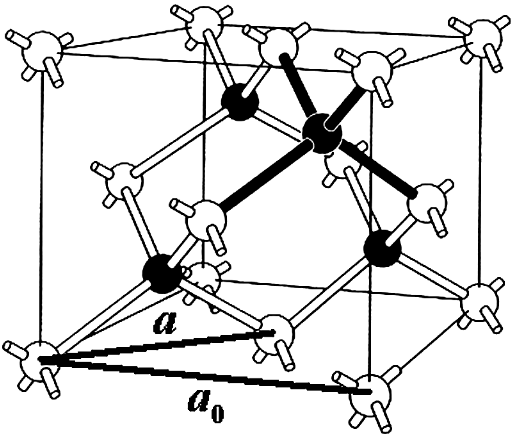

Fig.2.1. *Ball and stick model of the diamond lattice. Each atom is bonded to two pairs of atoms in the other sublattice with a tetrahedral bonding configuration. Atomic layers parallel to the (100) plane (the top plane of the cube) are separated by $a_0/4$ where a_0 is the bulk lattice constant. The lattice constant of the (100) surface is a. Modified from ref. [1].*

The bulk truncated (100) surface has two dangling bonds (sp^3-hybrid orbitals) per surface atom, which is an energetically unstable condition. The surface reconstructs by forming Si dimers, thus the number of dangling bonds per atom is reduced from two to one. Dimerization leads to the doubling of periodicity along the bond direction, ie, the surface exhibits a 2×1 structure. Even on nominally flat Si(100) surfaces, steps are formed spontaneously due to an anisotropic surface stress tensor; the surface is formed of terraces separated by steps which are a single atomic layer high. Because of the tetrahedral bonding configuration in the diamond lattice, the dimer direction is orthogonal on consecutive terraces, giving rise to the existence of both 2×1 and 1×2 domains. The surface reconstruction was first introduced by Schlier and Farnsworth in 1959 [2] when they observed a (2×1) low energy electron diffraction (LEED) pattern. Besides the 2×1 structure, other periodicities were found by diffraction methods: a c(4×2) structure by LEED [3, 4], and (2×2) and c(4×2) structures by He diffraction [5]. Several alternative models have been proposed for the reconstructed Si(100) surface: a vacancy model where half of the surface atoms are missing or a symmetric dimer model [2], a conjugated chain model where zig-zag chains are formed by the surface atoms [6, 7], an asymmetric dimer model [8, 9], and a dimer plus π-bonded chain model [10].

First real space scanning tunneling microscopy (STM) images in the mid 1980s by Tromp *et al.* [11] and Hamers *et al.* [12] evidenced the dimerized reconstruction showing the presence of both symmetric and asymmetric dimers at the surface. The debate as to weather the dimers were symmetric or asymmetric (ie, tilted) still remained. The surface dimer is bound by a σ bond formed from a pair of adjoining dangling bonds. The remaining two dangling bonds form a weaker π-like bond associated with an empty π^* orbital. In the two-dimensional surface, the π and π^* orbitals broaden into bands, which overlap in the case of symmetric dimers leading to a metallic surface. However, on the basis of photoemission studies [13 – 15], the surface has been found to be semiconducting. Therefore, either strong electron correlation effects or dimer tilting are required to open a gap between the occupied and unoccupied π surface states [16].

2.1. The asymmetric dimer model

The current consensus is that the dimers are asymmetric. The asymmetric dimer model is supported by a wealth of calculations [8, 9, 17 – 36], whilst some calculations favour the symmetric model [37, 38]. Tilted dimers have been demonstrated by several experimental methods as well [11, 12, 14, 31, 39 – 51].

The dimer tilting has two major consequences: Firstly, it opens up a Jahn-Teller-like gap between the electronic states located on the up- and down-atom; the sp^3 tetrahedral hybridization is distorted, so that the up-atom becomes more p-like, while the down-atom becomes more sp^2-like. This results in two dangling bond bands, an occupied D_{up} band, and an empty D_{down} band, yielding a semiconducting surface [52]. Secondly, the higher-order reconstructions can be formed by different configurations of alternating dimer-tilt directions. Alternate dimers can buckle in opposite directions giving a p(2×2) reconstruction. If alternate dimer rows are not in phase, then a c(4×2) structure is obtained. Ihm *et al.* showed that the 2×1 reconstruction was not the ground state of the Si(100) surface since a lower total energy was achieved with higher-order reconstructions such as p(2×2) and c(4×2), and predicted that an order-disorder phase transition would occur at around 250 K [22]. This phase transition was experimentally shown by Tabata *et al.* to occur at about 200 K from the c(4×2) to 2×1 [26]. The first low temperature STM images at 120 K by Wolkow showed the number of tilted dimers increasing at the expense of symmetric dimers and the existence of p(2×2) and c(4×2) domains [44]. The symmetric character of dimers in the STM images taken at room temperature (RT) is due to flipping of the dimer atoms between the up and down positions on a time scale much shorter than the STM measurement time [50, 53]. The structures of the Si(100) surface formed by asymmetric dimers and unit cells of 2×1, p(2×2), and c(4×2) reconstructions are presented in Fig. 2.1.1 (a). Figure 2.1.1 (b) shows an optimal geometry of the dimer.

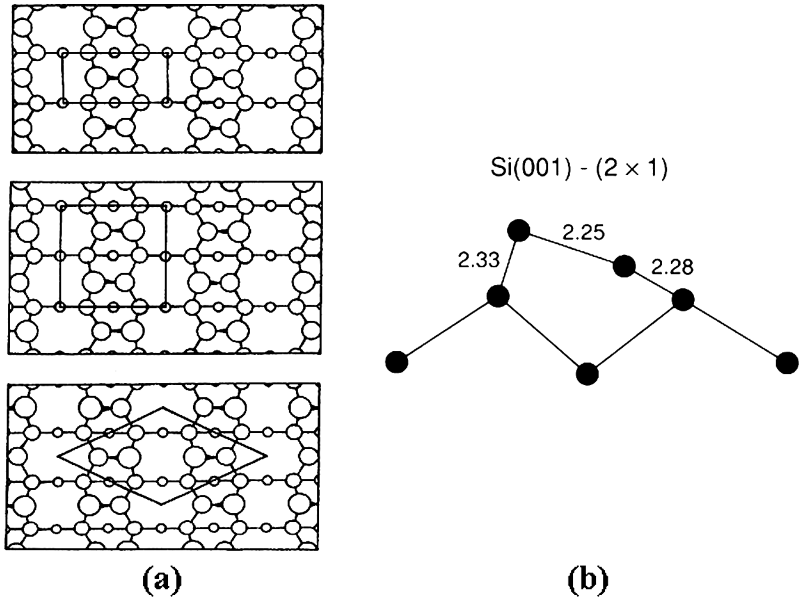

Fig. 2.1.1. *(a) Surface structure of the Si(100) formed by asymmetric dimers. The up and down dimer atoms are presented by large and small circles, respectively. From top to bottom, unit cells of 2×1, p(2×2), and c(4×2) reconstructions are indicated. From ref. [27]. (b) Optimised structure of the asymmetric Si(100)2×1 dimer model resulting from calculations by Ramstad et al. [33] and Krüger and Pollmann [35]. The bond lengths are given in Å, from ref. [52].*

The energy gain due to dimer formation is about 2 eV per dimer [33, 35] and the dimer tilting further lowers the total energy by 0.14 eV per dimer [35]. For the p(2×2) and c(4×2) reconstructions with alternating tilt directions, additional energy gains result from the interactions between neighbouring dimers along a dimer row (0.05 eV per dimer) and interactions of nearest neighbour dimers in two neighbouring dimer rows (0.003 eV per dimer) [33]. Therefore the c(4×2) reconstruction is lowest in energy.

2.2. Steps on the Si(100) surface

The dimer rows on the Si(100) surface run in orthogonal [011] directions, hence there are two distinct types of steps: the steps are aligned either parallel or perpendicular to the dimer row direction on the upper terrace. The step height on the Si(100) surface is typically quantized by single or double atomic layers. According to Chadi's notation [53], the single layer steps are called S_A and S_B, and the double layer steps D_A and D_B, where the subscripts *A* and *B* denote steps aligned parallel and perpendicular to the dimer rows on the upper terrace, respectively. Further, the S_B, D_A and D_B steps can be either non-rebonded or rebonded; the rebonded configuration saturates the dangling bonds at the step edge. The different step-edge configurations are seen schematically in Fig. 2.2.1.

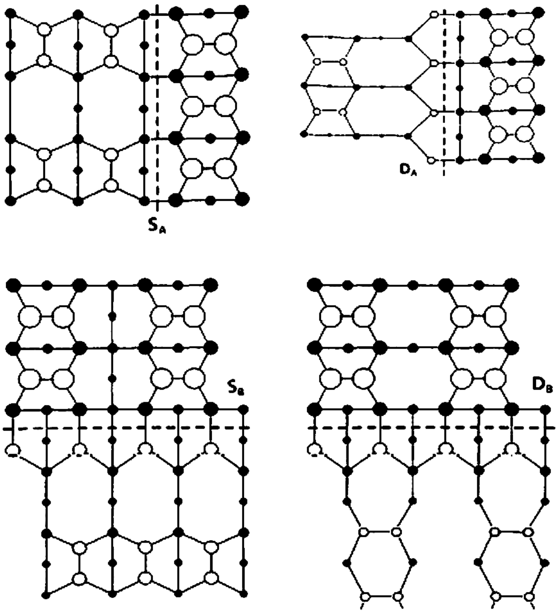

Fig.2.2.1. *Top views of step-edge configurations on the Si(100) surface [53]. Open circles denote atoms with dangling bonds and dashed lines indicate the step edge position.*

The step-edge formation energies were first calculated by Chadi [53] giving the following energies: 0.02 eV/2a (S_A), 0.30 eV/2a (S_B, rebonded), 0.10 eV/2a (D_B, rebonded), and 1.08 eV/2a (D_A). Similar results which agree in terms of the order of the formation energies have been obtained from other calculations [28, 31, 54 – 56] and measurements [57 – 59].

The Si(100) surface is intrinsically under anisotropic surface stress, σ; the stress is tensile along the dimer bond ($\sigma_{||}$) and compressive normal to the dimers ($\sigma_{\perp}$). The stress anisotropy ($\sigma_{||} - \sigma_{\perp}$) induces an ordered stress-domain structure, ie, a uniform single domain surface breaks up into a stripelike structure with steps separating alternating stress domains [60]. Therefore, the nominally flat surface exhibits terraces of width L separated by S_A and S_B steps. The surface tends to minimize its energy with smaller L, which is set against the energy cost due to the generation of more boundaries and so the surface configuration is a balance between these competing terms. The energetically favourable S_A steps are straight, whereas the S_B step edges are rough and contain kinks [57].

Vicinal surfaces, which are slightly miscut in the [011] directions, are formed by regular arrays of (100) terraces and steps that accommodate the misorientation. One would expect, by looking at the step formation energies, that the vicinal surface at equilibrium would consist of only double layer steps. However, the vicinal Si(100) surfaces exhibit a sequence of orientational phase transitions. For very small miscut angles, < 0.03°, a hill and valley structure with a step loop is observed [61]. In the range 0.03 – 0.1°, phases of wavy steps and relatively straight steps coexist [62]. From 0.1° up to 2°, the single-layer steps S_A and S_B alternate and the major phase transition from single layer steps to double layer steps occurs at around 2° [63 – 66]. The fraction of double layer steps increases gradually with an increasing miscut angle, as pairs of single layer steps collapse into double layer steps; there is no abrupt transition at a given critical miscut angle or a coexistence of spatial regions of single and double layer steps [67, 68]. At about 4° the surface contains predominantly double layer steps, which are always of the type D_B due to the high formation energy of the D_A steps, thus exhibiting a single domain 2×1 reconstruction. Figure 2.2.2. shows STM images of the Si(100)2×1 surface misoriented 0.5° and 4° in the [011] direction.

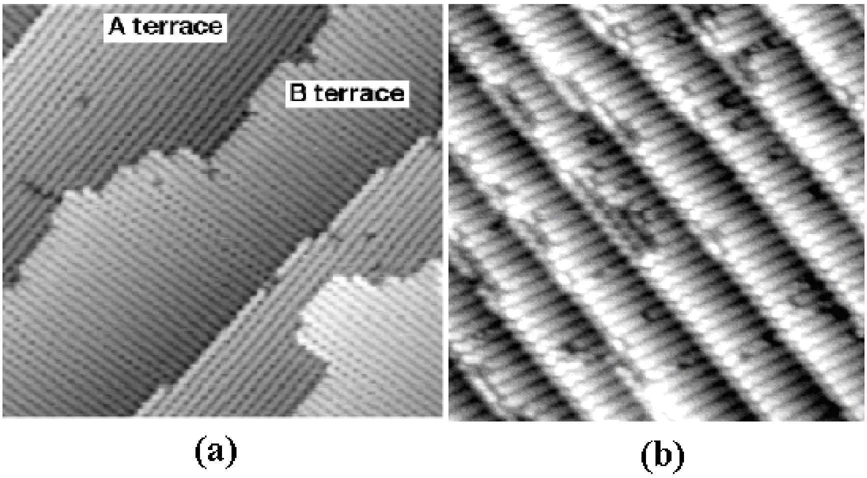

Fig. 2.2.2. *Scanning tunneling microscope image of vicinal Si(100) surface miscut towards the [011] direction. (a) Double domain reconstruction where straight S_A and rough S_B steps alternate for a small miscut angle of 0.5°. Filled state image (29×29 nm^2) taken at 196 K shows partial c(4×2) ordering, from ref. [69]. (b) Single domain 2×1 reconstruction with D_B steps for the miscut angle of 4°, empty state image (20×20 nm^2) taken at RT.*

Step bunching occurs on the vicinal Si(100) surface either after DC heating for about 100 hours at high temperature (~1000 °C) or after induction by adatom adsorption [70]. On a relatively flat surface, when the heating current is applied in a step-down direction, the terraces with dimers oriented perpendicular to the current expand, while in the case of a step-up current, the terraces with dimer orientation parallel to the current expand. On surfaces with narrow terraces, the step-up DC heating induces step bunching [71]. Adsorption of Au induces a “hill-and-valley” reconstruction with (119) facets [72] and adsorption of Ag leads to the formation of multiple double steps [73].

2.3. A thermodynamic description of the Si(100) surface

Surfaces can be described using Gibbs’ thermodynamic formalism. The thermodynamic behaviour of surfaces is governed by the surface free energy, which depends on energetic parameters related to the steps: step free energy, kink creation energy, and step-step interactions [74]. The surface free energy can also be expressed as a function of macroscopic parameters (see Fig.2.3.1): the miscut angle θ and its orientation ϕ, and the temperature T. The surface free energy per unit area $\gamma(\theta,T)$ is

$$\gamma(\theta,T)=\gamma(0,T)+\frac{f(T)}{d}|\tan\theta|+q(T)|\tan\theta|^3, \qquad (2.3.1)$$

where $\gamma(0,T)$ is the surface free energy per unit area for the low-Miller-index surface, d is the step height, $f(T)$ is the free energy per unit length for forming a step of height d, and $q(T)|\tan\theta|^3$ is the energy cost per unit area due to step-step interactions [74]. Here only steps running along a high-symmetry direction are considered. However, both the functions $f(T)$ and $q(T)$ depend also on the angle ϕ, ie, deviations of the step edge direction from the high-symmetry direction. Williams *et al*. have developed theories of statistical mechanical to describe the surface free energy by step-related parameters, as presented in detail in a review by Jeong and Williams [75].

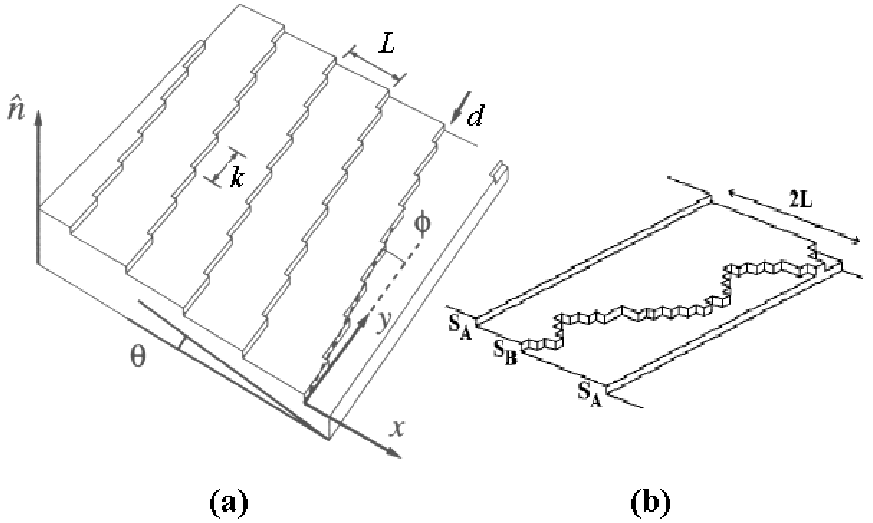

Fig.2.3.1. *(a) Vicinal surface (with respect to a low-Miller-index surface) composed of steps and kinks. Parameters used for description of surface energetics are indicated: the misorientation angles ϕ and θ, the average distance between neighbouring steps L, the kink length k, and the kink height d. Modified from ref. [1]. (b) The Gruber-Mullins model applied to the Si(100) surface. A meandering S_B step edge is trapped between the hard walls formed by two neighbouring straight S_A step edges, from ref. [74].*

Formation energies of step edges and kinks

At zero temperature, steps contain forced kinks to accommodate the misorientation with respect to high-symmetry axes. At higher temperatures, thermally induced kink pairs appear. There are two types of kinks along the step edge: those pointing towards the lower terrace (positive kinks) and those pointing towards the upper terrace (negative kinks). The unit of the kink length, k, in the step edge of the Si(100) surface is $2a$ (a = 3.84 Å) and, in general, kinks are formed in units of two dimers, ie, with a (2×2) lattice. At any point on the step, the normalization condition holds:

$$n_0 + \sum_{k=1}^{\infty} \left(n_{+k} + n_{-k} \right) = 1, \tag{2.3.2}$$

where $n_{\pm k}$ denotes the probability that there is a positive or negative kink of length $2ak$ [74]. The equilibrium structure of an anisotropic Si(100) surface for a single layer S_A (S_B) step can be expressed using the relations

$$\varepsilon_{\parallel(\perp)} / k_b\, T = -\ln\left(\frac{n_{+1} n_{-1}}{n_0^2} \right) \text{ and} \tag{2.3.3}$$

$$\delta / k_b T = -\ln\left(\frac{n_{\pm r} n_0}{n_{\pm(r-1)} n_{\pm 1}} \right), \ r \geq 2, \tag{2.3.4}$$

where $\varepsilon_{\parallel(\perp)}$ refers to the nearest-neighbour interaction in a unit building block $(2a \times 2a)$ along (perpendicular to) the substrate-dimer-row direction, and δ refers to the second-nearest-neighbour interaction [76]. The following values have been found: $\varepsilon_{\perp} = (3.6 \pm 0.2) k_b T_f$, $\varepsilon_{\parallel} = (5.7 \pm 0.3) k_b T_f$, and $\delta = -(1.0 \pm 0.3) k_b T_f$, where T_f is the temperature where the step roughness is frozen [76]. Further [74], the step edge formation energy for an S_A (S_B) step is then

$$E_{S_A} = \frac{\varepsilon_{\perp}}{2} + \delta, \tag{2.3.5}$$

$$(E_{S_B} = \frac{\varepsilon_{\parallel}}{2} + \delta), \tag{2.3.6}$$

and the kink formation energy for a kink of length k is

$$E_{kink,S_A} = k \frac{\varepsilon_{\parallel}}{2} + (k-1)\delta = kE_{S_B} - \delta, \ k \geq 1, \tag{2.3.7}$$

$$(\ E_{kink,S_B} = k \frac{\varepsilon_{\perp}}{2} + (k-1)\delta = kE_{S_A} - \delta, \ k \geq 1\ ). \tag{2.3.8}$$

The formation energies of double-layer step edges and their kinks can be determined similarly [59].

Step-step interactions

Step interactions arise from entropic and energetic origins. The entropic repulsive interaction emerges since step cannot cross one another. The Gruber-Mullins model [77] of a meandering step trapped between two hard walls (see Fig. 2.3.1), can be applied to the Si(100) surface, so that the S_B and S_A steps correspond to the meandering step and the hard wall, respectively. Each step-step collision decreases the number of configurations available per step by a factor of 2 and thus reduces the entropy by $k_b$ln2. The mean-square length of a kink in an S_B step is [78]:

$$\left\langle k^2 \right\rangle = \frac{\sum_{k=-\infty}^{\infty} k^2 e^{-E_{kink,S_B}(k)/k_b T}}{\sum_{k=-\infty}^{\infty} e^{-E_{kink,S_B}(k)/k_b T}}. \tag{2.3.9}$$

For an average spacing L between neighbouring steps, the average distance between successive collisions is $L^2 / \left\langle k^2 \right\rangle$. The increase in free energy per unit step-edge length due to entropic repulsion is thus $\left\langle k^2 \right\rangle L^{-2} k_b T \ln 2$.

Energetically driven interactions due to the anisotropic surface stress tensor are predicted by elasticity theory which states that force dipoles along step edges lead to step formation energy contribution varying as L^{-2}, and that strain relaxation of stress across step edges leads to contribution varying as ln$L$. For large terrace widths, the strain relaxation step interactions (ln$L$) predominate over the direct step interaction (L^{-2}). The strain relaxation energy per unit step length for the single-layer stepped surface is [60, 64]:

$$E_{strain}(L) = -\frac{(1-\nu)}{2\pi\mu}(\sigma_{\parallel} - \sigma_{\perp})^2 \ln\left(\frac{L}{\pi a}\right) = -C\ln\left(\frac{L}{\pi a}\right), \qquad (2.3.10)$$

where v is the Poisson ratio (of Si), μ is the bulk modulus (of Si), and a is the microscopic cutoff length (ie, the surface lattice constant). The orientational transition from a single-layer-stepped surface to a double-layer-stepped surface is understood by considering the step-edge free energy difference, Δf, between the surfaces. Besides the step-edge free energies of pairs of single layer steps ($f_{S_A} + f_{S_B}$) and of a double layer step (f_{D_B}), the contribution of the strain relaxation term is taken into account (strain relaxation does not occur on the single-domain double-layer-stepped surface), giving the free energy difference of [74]

$$\Delta f = f_{S_A} + f_{S_B} - 2C\ln\left(\frac{L}{\pi a}\right) - f_{D_B}. \qquad (2.3.11)$$

For a sufficiently large L, the strain relaxation term stabilizes the single-layer-stepped surface.

2.4. Defects on the Si(100) surface

Surface defects may affect reactions on the surface, for example adsorption and desorption, epitaxial growth and surface diffusion. Linear defects in the form of steps are intrinsically present at the Si(100) surface. Another type of defect is missing dimers, which according to STM measurements, are dispersed over the surface typically covering a few percent of the total surface area. The defects are classified as single missing dimers, double missing dimers, and double missing half-dimers and are labeled as A, B, and C-type defects, respectively [79]. Alternatively, the A and B-type defects are called 1-DV and 2-DV, where DV refers to dimer vacancy [80]. The more complex C-type defect is revealed to be due to dissociative adsorption of water molecules [81, 82]. The defects can form complexes of several DVs or an ordered 2×n phase, where the DVs align themselves perpendicular to the Si dimer rows forming trenches which are separated by n Si dimers, n typically being between six and ten [83]. Such a reconstruction is often related to a very small amount of Ni contamination [84, 85] and occurs also for Ge overlayers on Si(100) [86, 87].

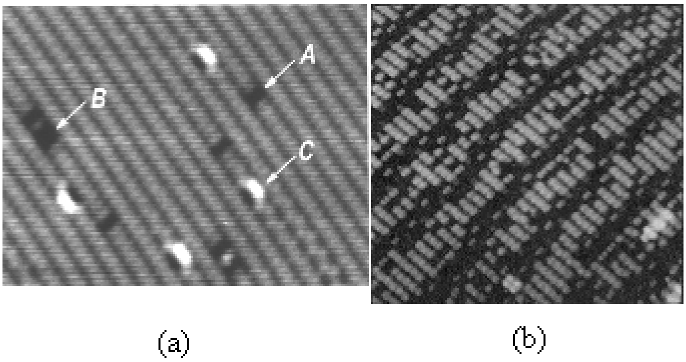

Fig. 2.4.1. *STM images showing defects on the Si(100) surface: (a) A, B, and C-type defects [79] and (b) an ordered 2×n phase formed by defect vacancy lines [83].*

3. Experimental methods

3.1. Low energy electron diffraction (LEED)

Low energy electron diffraction (LEED) is the oldest diffraction technique applied to surfaces. It was first used in electron scattering experiments on nickel by Davisson and Germer in 1927 [88]. Electrons, as charged particles, interact strongly with matter and their mean free path in a solid is short. The typical kinetic energy of electrons in LEED is between 20 and 300 eV, which corresponds to the minimum in the curve of mean free path, see Fig. 3.3.5. Thus LEED is a surface sensitive probe. According to the de Broglie relation, the wavelength of electrons, λ, is

$$\lambda(\text{Å}) = \frac{h}{p} = \frac{h}{mv} = \frac{h}{\sqrt{2mE}} \approx \sqrt{\frac{150}{E(\text{eV})}}, \tag{3.1.1}$$

where h is Planck's constant, p is the momentum, m is the mass, v is the velocity, and E is the energy. It can be seen from eq. (3.1.1) that the energy of electrons in LEED fits into the range of distances between atoms in solids (≈1 Å) and therefore interference of the electrons and the solid surface is expected. The incident and scattered electrons are presented by wave vectors $\boldsymbol{k_0}$ and $\boldsymbol{k'}$, respectively. The magnitude of the wave vectors is

$$|k| = \frac{2\pi}{\lambda}, \tag{3.1.2}$$

and hence $k = p/\hbar$.

The scattering process can be visualized using the Ewald sphere construction in reciprocal space (Fig. 3.1.1), which is reduced into two dimensions since the scattering occurs only in the upper-most atomic layer(s). The reciprocal lattice vectors ($\boldsymbol{a}^*$, $\boldsymbol{b}^*$) are defined relative to their real-space counterparts ($\boldsymbol{a}$, $\boldsymbol{b}$):

$$\boldsymbol{a}^* = \frac{2\pi}{\boldsymbol{a}}, \boldsymbol{b}^* = \frac{2\pi}{\boldsymbol{b}} \ . \tag{3.1.3}$$

Thus distances in the reciprocal space are directly proportional to momentum [89]. The criteria for constructive interference for the elastically scattered electrons is that the change in the electron wave vector must be equal to a reciprocal lattice vector $\boldsymbol{g}$ given by

$$\boldsymbol{k}' - \boldsymbol{k_0} = \boldsymbol{g} = h\boldsymbol{a}^* + k\boldsymbol{b}^* \ (h,k = 0,1,2..). \tag{3.1.4}$$

Equation (3.1.4) is called the Laue condition for diffraction. In elastic scattering $|k'| = |k_0|$; only the direction of the wave vector is changed, not the magnitude. The Ewald sphere construction is made by placing a sphere of radius $|k_0|$ into the reciprocal lattice. The vector $\boldsymbol{k_0}$ begins at the centre of the sphere and ends at an arbitrary lattice point. The Laue condition is satisfied when the scattered wave vector, $\boldsymbol{k'}$, ends on a reciprocal lattice point on the sphere. The LEED pattern is a reflection of reciprocal space. Changing the incident electron energy changes the radius of the sphere; an increase in energy increases the number of LEED spots on the screen. Usually the incident beam is normal to the surface, thus the LEED pattern is symmetric and converges towards the (0,0) specular beam when the energy is increased.

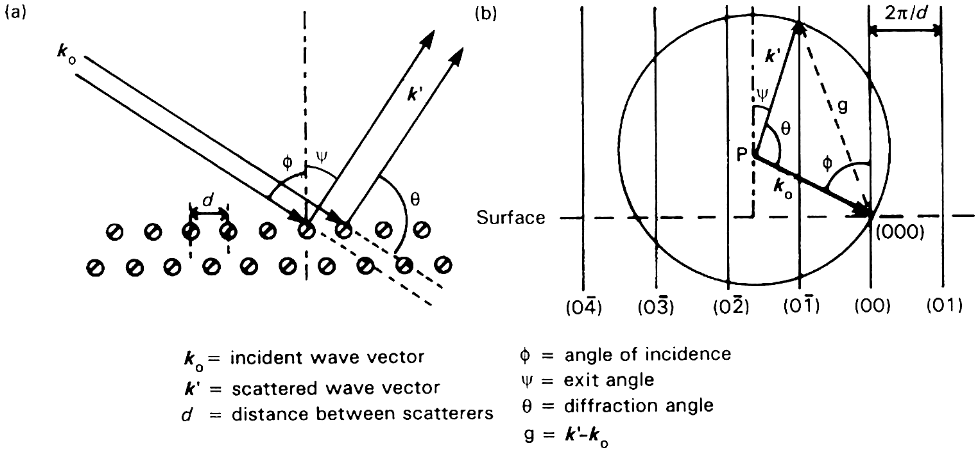

Fig.3.1.1. *Diffraction process occurring at a surface in real space (a) and corresponding two-dimensional Ewald sphere construction in reciprocal space (b). From ref. [89].*

A schematic illustration of typical display-type LEED apparatus is shown in Fig. 3.1.2. The electrons are emitted from a cathode, collimated by a lens system, accelerated to the desired energy, and finally come out from a drift tube. The electron beam is nearly monoenergetic and hits the sample surface at normal incidence. The detector consists of hemispherical concentric grids. The first grid, the sample, and the drift tube are grounded so that there is a field free region between the sample and the first grid. The second and third grids are at a negative potential slightly lower than the primary electron energy so as to repel the inelastically scattered electrons. The fourth grid is grounded and, after passing it, the elastically scattered electrons are accelerated towards the fluorescent screen with a positive voltage [90]. In the screen, the positions of the interference maxima form the diffraction pattern.

LEED has become a standard laboratory technique since one short LEED experiment rapidly gives information about the surface order and quality. When the surface is reconstructed or covered with adsorbates, analysis of the LEED patterns using the simple geometric theory of diffraction (ie, determination of the directions of the interference maxima) can be used to determine the surface symmetry and unit cells of the periodic structures. As well as gaining a simple geometric interpretation, the intensities of the LEED spots can be measured. In the spot profile analysis method (SPA-LEED) variations of the intensities of the diffracted beams with angle near the preferred directions are analysed using kinematic theory giving information about partial disorder on the surface [91]. A complete structural analysis is obtained from the *I*/*V*-spectra, which measure the intensity of each diffracted beam as a function of the primary electron energy. Atomic positions within the unit cell can be determined from the *I*/*V*-spectra. However, the quantum mechanical treatment with dynamic theory is essential in the analysis due to the multiple scattering effects [see e.g. 92, 93].

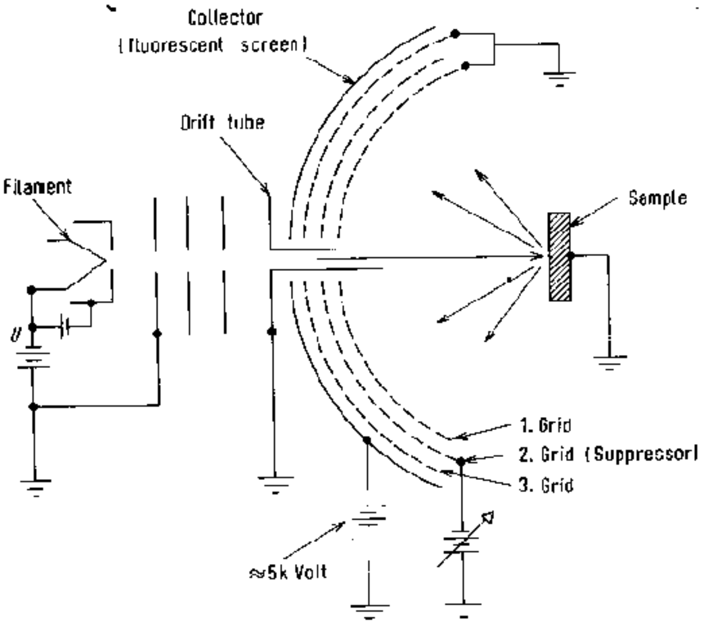

Fig. 3.1.2. Schematic illustration of a typical display-type LEED apparatus. Principle of operation is described in the text. From ref. [90].

3.2. Scanning tunneling microscopy/spectroscopy (STM/STS)

Scanning tunneling microscopy (STM) was invented by Binnig and Rohrer in 1981 [94 – 96]. Nowadays STM is widely applied in surface science since it offers real space information of structural and electronic properties of the surface, including non-periodic structures, with atomic resolution. It is based on quantum mechanical tunneling of the electron wave function through a potential barrier. The operation technique of STM is simple: a sharp tip is scanned across the sample surface. When a small bias voltage, *V*, is applied between the tip and the sample, and the tip is brought close enough to the sample, electron tunneling through the vacuum becomes possible and a tunneling current, *I*, starts to flow. The current flows from the tip to the sample or vice versa, depending on the bias polarity; for positive *V* (in reference to the sample) the unoccupied states of the sample are probed and for negative *V*, the occupied states. The principle is shown schematically in Fig. 3.2.1. Obviously, both the tip and the sample need to be semiconductors or conductors. The distance, *d*, between the tip and the sample is typically ≈1 nm. The STM image is commonly acquired as a constant current topography (CCT), where a feedback circuit system is used to keep the tunneling current constant at the chosen bias voltage and the image is constructed by plotting the changes in the sample height versus the tip position over the sample.

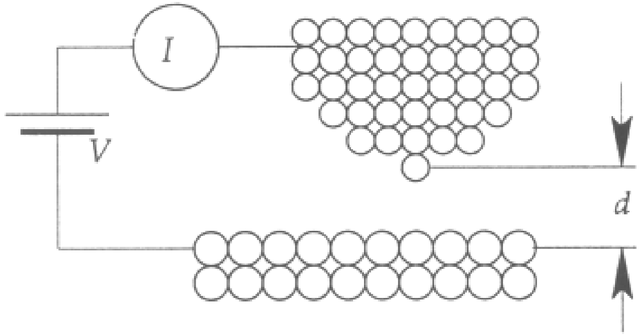

Fig. ***3.2.1.*** *The principle of STM. A tunneling current I starts to flow when bias voltage V is applied between the tip and sample separated by a small enough distance d. From ref. [1].*

The tunneling effect is shown in Fig. 3.2.2. Two electrodes with a work function φ are separated by a vacuum gap. Inside the electrodes, the wave functions of states are periodic. Outside, these wave functions decay exponentially with distance into the vacuum, with a decay length of $\kappa^{-1} = \left(2m\varphi / \hbar^2\right)^{-1/2}$ [1]. When the electrodes are brought close together, with distance *d*, the overlap of the decaying wave functions becomes large enough to facilitate the tunneling. Under an applied voltage, a measurable current *I* is generated, which is given by [89]

$$I \propto e^{(-2\kappa d)}. \tag{3.2.1}$$

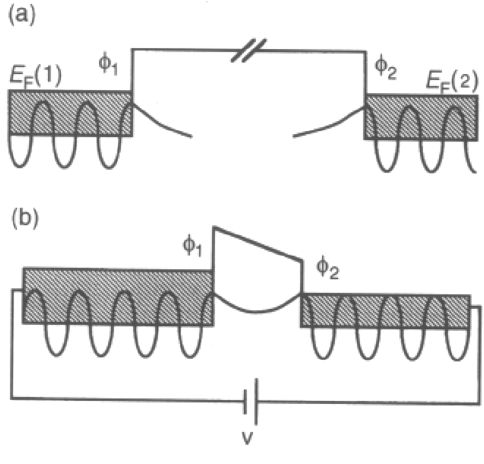

Fig. ***3.2.2.*** *The tunneling effect. When the distance between electrodes 1 and 2 is large, as in (a), the electron wave functions decay into the vacuum, whereas at a sufficiently short distance the tunneling occurs between the electrodes (b), from ref. [89].*

The essential quantity for theoretical treatment of STM is the tunneling current. However, the one-dimensional model above is not adequate to describe the complex interaction between the tip and sample. A widely used model, due to Tersoff and

Hamann [97], relates the observed atomic corrugation to the local density of states of valence or conduction electrons. Lang presented calculations in which the effect of an adatom on the surface was taken into account [98]. Tsukada *et al.* introduced simulations which included the electronic states of both the sample and the tip [99]. In the model of Tersoff and Hamann, the tunneling current I is expressed with the Bardeen's equation [100]. Assuming that the tip is a point probe and in the limit of a small sample bias voltage and low temperature, the local tunneling current is reduced to [97]

$$I \propto \sum_{\nu} \left|\Psi_{\nu}(\bar{r}_0)\right|^2 \delta(E_{\nu} - E_F), \tag{3.2.2}$$

where E_{ν} is the energy of the state Ψ_{ν} of the sample surface. The right hand side of eq. (3.2.2) is the local density of states (LDOS) at the Fermi level E_F at position $\bar{r}_0$ of the point probe. Thus the STM image in this case is a contour map of constant surface LDOS. An important question which arises when trying to interpret STM images is how these images are related to the position of atoms at the surface; the topographic image is a convolution of electronic and geometric properties of the sample surface.

The atomic scale resolution of STM results from the exponential dependence of I on the barrier thickness. The probability of achieving tunneling changes by almost an order of magnitude for a one angstrom change in the barrier width [89, 101]. Furthermore, due to this exponential dependence, the tunneling current will mainly flow through the leading atom at the end of the tip, thus providing an atomically sharp tip apex. The effect is illustrated in Fig. 3.2.3. In experiments, the ideal tip configuration is not accomplished leading to artifacts in the STM images: a multiple tip causes multiplied imaging, a dull or dirty tip makes all the features in the image look the same, contamination of the tip by the sample causes streaking and a loss of resolution, and improper adjustment of feedback parameters produces tails or shadows if the tip cannot trace protrusions on the surface.

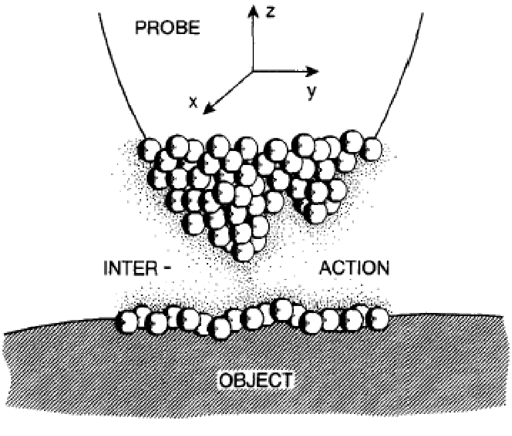

Fig. 3.2.3. *The tunneling current decays exponentially as a function of the separation between the sample and tip. In the case of multiple atoms on the tip apex, the current flows mostly through the leading atom, thus providing the atomic resolution of STM. From ref. [101].*

In the spectroscopic mode of operation, STM has the significant advantage of providing information at atomic spatial resolution. Other surface spectroscopy techniques, such as ultraviolet photoemission spectroscopy (UPS), inverse photoelectron spectroscopy (IPES), and electron energy loss spectroscopy (EELS), give information averaged over a large surface area, whereas in STM the tunneling comes from specific locations with an area typically 5 Å in diameter [101, 102].

Spectroscopic operation of STM can be utilized using several techniques. In voltage dependent imaging conventional topographic STM images (CCTs) are acquired at different bias voltages. Essentially qualitative information is obtained by comparing images taken from the same area as a function of the bias voltage. When a voltage V is applied on the sample, the states lying within an energy window $\left|E_\mathrm{F} - eV\right|$ contribute to the tunneling. In particular, for semiconductors, the images taken near either side of the bandgap are dominated by distinct surface states revealing the relationship between the occupied and unoccupied states.

Modulation techniques, the most common example of which is scanning tunneling spectroscopy (STS), measure $\mathrm{d}I/\mathrm{d}V$ simultaneously with the surface topography. In such techniques, a high-frequency modulation voltage is applied with a constant bias voltage and the component of the tunneling current which is in phase with the applied modulation is measured; the average tunneling current is kept constant [89]. The constant average tunneling current causes $1/V$ dependence on $\mathrm{d}I/\mathrm{d}V$, which makes it difficult to use at low voltages. Also, STS cannot probe the electronic structure of states near E_F, which is often of primary interest in studies of semiconductors [102].

In a method which Hamers *et al.* [103] called Current Imaging Tunneling Spectroscopy (CITS), in addition to obtaining a topographic image, the tunneling I-V curve is measured at each location during the raster scan over the surface. Using a sample-and-hold technique, the feedback control system is switched on and off. When the feedback loop is locked, the applied bias voltage is rapidly ramped through an energy interval (for example from – 2 V to + 2 V), and the tunneling I-V curve is measured. The feedback loop is then reactivated to re-establish the original conditions of topographic imaging, ie, a constant stabilization voltage V_stab and the adjustment of tip height to maintain a constant current [101, 102]. The value of V_stab influences I-V curves since the sample-tip separation may be different at each location. Therefore, the spectroscopic data is usually represented by normalized $(\mathrm{d}I/\mathrm{d}V)/(I/V)$ curves. Normalization of the differential conductivity by the total conductivity removes, to a great extent, the exponential dependence on voltage and sample-tip separation [104].

In addition to imaging surfaces, STM is nowadays used for atomic-scale manipulation of surfaces. Single atoms and molecules can be manipulated to create artificial structures, which can be characterized *in situ* by STM/STS, thus providing insights into physical and chemical phenomena at an atomic level. The manipulation can be induced by controlling tip-sample interactions, tunneling electrons or electric field between the tip and the sample.

In lateral manipulation, a particle at the surface is moved with the tip along the substrate surface without loosing contact with the substrate. The tip is brought very close to the particle, so that, as well as the weak van der Waals interactions, chemical forces between tip and particle are also induced [105]. Lateral manipulation was first demonstrated by Eigler and Schweizer in 1990 when they wrote the “IBM” logo with Xe atoms on a Ni(110) surface [106]. In vertical manipulation, a particle is transferred from the surface to the tip and vice versa. The transfer process can be realized by using an electric field between the tip and the sample, or by exciting with inelastic tunneling electrons, or by making tip-atom/molecule mechanical contact [107]. The electric field induced manipulation is performed by changing the polarity of the applied bias voltage; an atom/molecule having a dipole can experience either an attractive or repulsive force from the tip [107]. In inelastic electron tunneling induced manipulation processes, controlled excitations of atoms and molecules can be performed. Low energy electrons or holes are injected from the tip to a target atom/molecule on the surface and the tunneling electron energy is transferred to the target through a resonance state leading to various excitations [107].

With an appropriate manipulation technique, or combination of several techniques, it is possible to create molecular switches, contacts and engines [105], or to investigate individual steps of a chemical reaction as in the so-called Ullmann reaction where dissociation, diffusion, and association have been realized in a step-by-step manner [108].

3.3. Synchrotron radiation photoelectron spectroscopy (SR-PES)

3.3.1. Synchrotron radiation

Electromagnetic radiation emitted by a charged particle (electron or positron) moving along a circular orbit at relativistic speed is called synchrotron radiation. In a typical synchrotron radiation source the electrons are injected into a storage ring from a linear accelerator and then follow a path determined by magnetic fields. In the storage ring, the path of electrons contains straight sections between the curved areas. Three types of magnetic devices are generally used to generate the synchrotron radiation: bending magnets in the curved areas, and wigglers or undulators, which are periodic magnetic structures inserted in the straight sections. The energy lost to synchrotron radiation is returned to the electrons when they pass a radio frequency cavity after each circle.

The angular distribution of radiation emitted by an electron in a circular orbit is, in the classical case, spread over a large range of angles. In the relativistic case, when the velocity of electrons approaches the speed of light the angular distribution of radiation is concentrated in a narrow cone tangential to the orbit (Fig. 3.3.1). Figure 3.3.2 illustrates the radiation produced in the different types of magnetic systems.

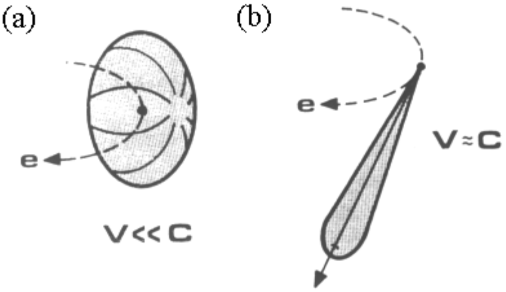

Fig.3.3.1. *The angular distribution of radiation emitted by an electron in the classical case (a) and in the relativistic case (b) [109].*

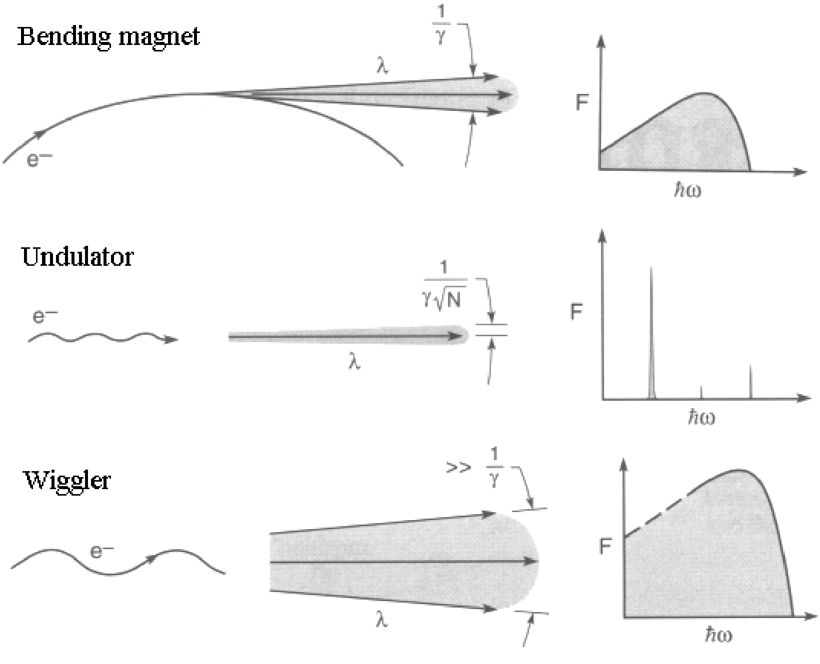

Fig.3.3.2. *Synchrotron radiation produced by bending magnets, undulators, and wigglers. On the left, the trajectory of an electron in the magnetic field is shown, in the middle the angular distribution of the radiation is presented and compared to the angular width of the natural radiation cone, 1/γ, and on the right the radiation spectrum is seen. From ref. [110].*

The superiority of synchrotron radiation to other radiation sources is due to its unique properties [109 – 111]:

(i) A wide spectral distribution. The photon energy range is $10^{-1} – 10^{5}$ eV, which corresponds to wavelengths $10^{3} – 10^{-1}$ Å. The energy is tunable, which enables one to adjust the surface sensitivity.

(ii) A high intensity and collimation to a small area. The measuring time is short and even trace amounts of elements can be observed.

(iii) Polarization. The radiation is linearly polarized in the plane of the orbit and elliptically polarized outside the plane of the orbit.

(iv) Time structure. The electrons travel in bunches so that the radiation is pulsed with high frequency.

3.3.2. Photoelectron spectroscopy

The photoemission process

Photoemission spectroscopy (PES) is based on the photoelectric effect first observed by Hertz in 1887 and explained by Einstein in 1905. The principle of PES is to measure the kinetic energy E_K of photoelectrons emitted from the sample after photon excitation; this in turn gives the binding energy E_B of the electron in the sample via the relation

$$E_K = h\nu - E_B - \phi, \tag{3.3.1}$$

where $h\nu$ is the photon energy and φ is the work function.

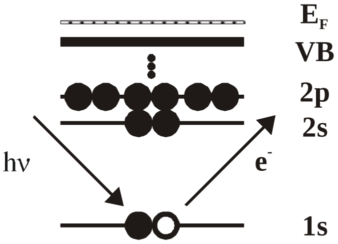

Fig. 3.3.3. *Schematic illustration of the photoemission process. The atom is excited by an incident photon (hν) and the excited state is relaxed upon emission of an electron from 1s level.*

The photoemission spectra from solids are commonly interpreted using the three-step model introduced by Berglund and Spicer [112, 113]. It divides the complicated photoemission process into three steps: the excitation of the photoelectron, its journey through the solid to the surface, and its penetration through the surface into the vacuum. The three-step model does not obey the uncertainty principle because it assumes that the optical excitation takes place at a given point in the solid before propagation and transmission into the vacuum, and that the inelastically scattered electrons lose their energy after the optical excitation. In the correct one-step model one considers the excitation from an initial state, which is a Bloch wave in the crystal, into a damped final state near the surface. The short mean free path of the electrons in the solid is taken into account by the damping. Such models are of importance to the interpretation in angle resolved PES experiments using low photon energies.

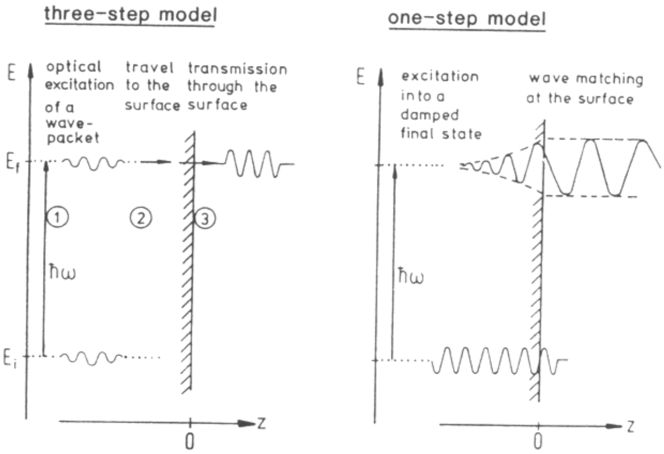

Fig. 3.3.4. *Illustration of three-step and one-step models [114].*

Surface sensitivity

Photoelectron spectroscopy is a surface sensitive technique since the mean free path of electrons in the solid, λ, is short. The dependence of λ on electron energy is presented by the "universal curve", Fig. 3.3.5. It is independent of the element and has a minimum at the energy range of 20 – 100 eV.

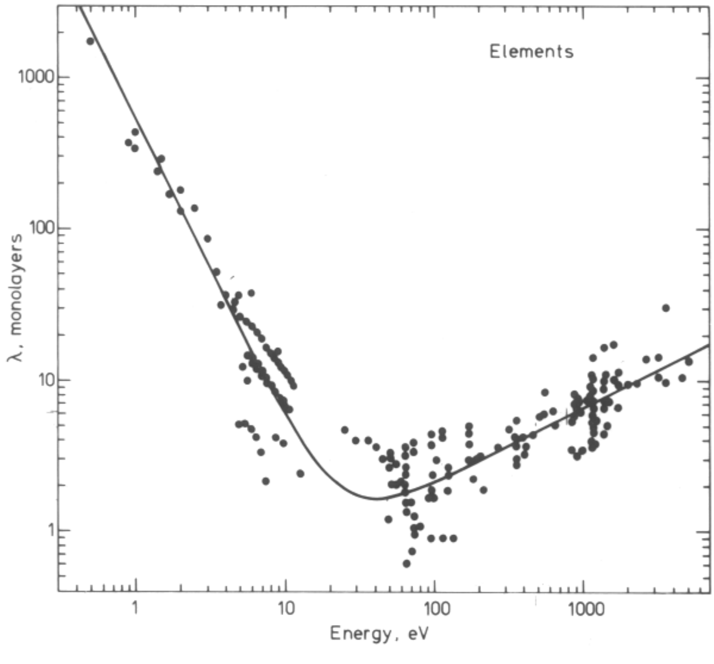

Fig. 3.3.5. *Mean free path of electrons vs. energy, the universal curve [115].*

The binding energy

The binding energy E_B of the photoelectron emitted from an N-electron system is the total energy difference between the final state, with $N - 1$ electrons, and the initial state with N electrons:

$$E_B = E_f(N-1) - E_i(N), \tag{3.3.2}$$

where $E_f(N - 1)$ is final state energy and $E_i(N)$ is the initial state energy. The energies are often considered as one-electron eigenvalues in terms of the Hartree-Fock model:

$$E_B = E_f^{HF}(N-1) - E_i^{HF}(N) + \Delta E^c, \tag{3.3.3}$$

where E^{HF} is the total energy in the limit of Hartree-Fock approximation (ie, the kinetic energy, Coulomb, and exchange terms of each individual electron are calculated as though all other electrons in the system form a static background [116]) and E^c is a correlation term to take into account all discrepancies between the real total energy and E^{HF}. According to Koopmans' theorem, based on the "frozen approximation", the binding energy is equal to the negative orbital energy $-\varepsilon_k$ of a level k (here k denotes the level from which the photoelectron is emitted):

$$E_B = -\varepsilon_k. \tag{3.3.4}$$

However, the assumption that the final state remains unaffected upon the photoemission fails; the electrons left in the system, which now contains a hole, rearrange to minimize their total energy. This relaxation effect can be considered in two parts: 1) an intra-atomic relaxation of the electrons on the atom itself and 2) an extra-atomic contribution from the screening caused by the surrounding atoms in the solid. The binding energy is, more accurately,

$$E_B = -\varepsilon_k - E^R(k) + \Delta E^c, \tag{3.3.5}$$

where $E^R(k)$ is the relaxation energy of orbital k [116].

A core-level chemical shift gives rise to differences in binding energies of the same atom in different chemical states, e.g., oxidation state, lattice site, or molecular environment [90, 115, 117]. The chemical shift effect can be interpreted in terms of initial state effects using the charge potential model. The binding energy difference ΔE_B of an atom i in two different valency states 1 and 2 is written as

$$\Delta E_B = E_B(2) - E_B(1) = K[q_i(2) - q_i(1)] + [V_i(2) - V_i(1)], \tag{3.3.6}$$

where K is a proportionality constant, q_i is the valence charge, and $V_i = \sum_j q_j / r_{ij}$ is a potential (often called the Madelung potential) arising from charges q_j centred at positions r_{ij} relative to atom i [90]. In covalent solids the Madelung potential is weak and short ranged, but in ionic solids it becomes significant. The Madelung term is opposite in sign to the valency charge term, thus it decreases the chemical shift. The amount of chemical shift is typically a few eV. In cases where screening differs from one chemical environment to another, the final-state contributions to the chemical shift become noticeable and a term $\Delta E^R = E^R(2) - E^R(1)$ should be added in order to describe the difference in relaxation energies E^R.

In addition, other effects may contribute to the observed binding energy, for example band bending at semiconductor surfaces, shake-up and shake-off satellites, incomplete screening, or multiplet splitting.

Surface core level shifts

Surface core level shifts (SCLS) are the binding energy differences between the atoms at the surface and those in the bulk, typically of the order of a few tenths of an eV. They are associated with the reduced coordination at the surface, and thereby the dissimilar valence properties of the surface and bulk atoms. After being first observed in 1978 [118], the importance of SCLS in surface studies has increased significantly. In particular, adsorption of foreign atoms on the surface modifies the chemical environment of the neighbouring surface atoms, leading to additional core level lines. In the spectrum, there should be as many lines as inequivalent substrate sites since a given core level shift corresponds to a given chemical environment.

One way to describe the SCLS is using a formalism introduced by Williams and Lang [119] and further developed by Spanjaard *et al.* [120]. The measured SCLS (denoted as Δ^{SB}) is given by

$$\Delta^{SB} = \left[E^S(N-1) - E^S(N)\right] - \left[E^B(N-1) - E^B(N)\right], \tag{3.3.7}$$

where $E^{S(B)}(N)$ is the total energy of the system in the surface (bulk) expressed as a function of the number of the electrons (N) in a particular core level. By expanding the total energies to a Taylor series and using the density functional formalism, we will get two contributions:

$$\Delta^{SB}_{conf-chem} = \varepsilon^B - \varepsilon^S \tag{3.3.8}$$

and

$$\Delta^{SB}_{relax} = \frac{1}{2}\frac{\partial}{\partial N}\left[\left(\varepsilon^S - \varepsilon^B\right) + \ldots\right]. \tag{3.3.9}$$

The equation (3.3.8) is just Koopmans' theorem, which includes the changes in configuration and chemical environment before the photoelectron is emitted from the atom. The equation (3.3.9) accounts for all other contributions to the SCLS, ie, the final state effects induced upon the core hole formation.

Another approach to the SCLS phenomenon has been introduced by Johansson and Mårtensson [121] based on thermodynamical quantities. In the thermodynamical model, it is assumed that the core hole is fully screened and the screening electron occupies the lowest unoccupied valence state. Moreover, it is assumed that a fully screened atom of nuclear charge Z with a deep core hole (denoted by Z^*) can be replaced by a neutral atom of nuclear charge Z+1 (equivalent-core approximation). Under these assumptions, a Born-Haber cycle is used to calculate the binding energy shift between bulk and free atoms or between bulk and surface atoms. Figure 3.3.6. shows the Born-Haber cycle for SCLS of clean metal surfaces. A starting point is Z-metal with $N=N_S+N_B$ atoms [$N_{S(B)}$ is the number of surface(bulk) atoms], which are removed from the metal. From a friction x of these atoms, the core electron is removed. These Z^*-ions are neutralized by adding a valence electron. Two metals are built up from the Z and Z^*-atoms, finally the two metals are mixed and the Z^*-atoms are considered as impurities in the Z-metal. The equivalent-core approximation is used to replace the Z^* by Z+1. We have for the shift between a surface atom and bulk atom

$$\Delta^{SB} = E_S^{Z+1} - E_S^Z, \tag{3.3.10}$$

where E_S is the variation of energy per surface atom, induced by the creation of the surface, and related to the surface tension.

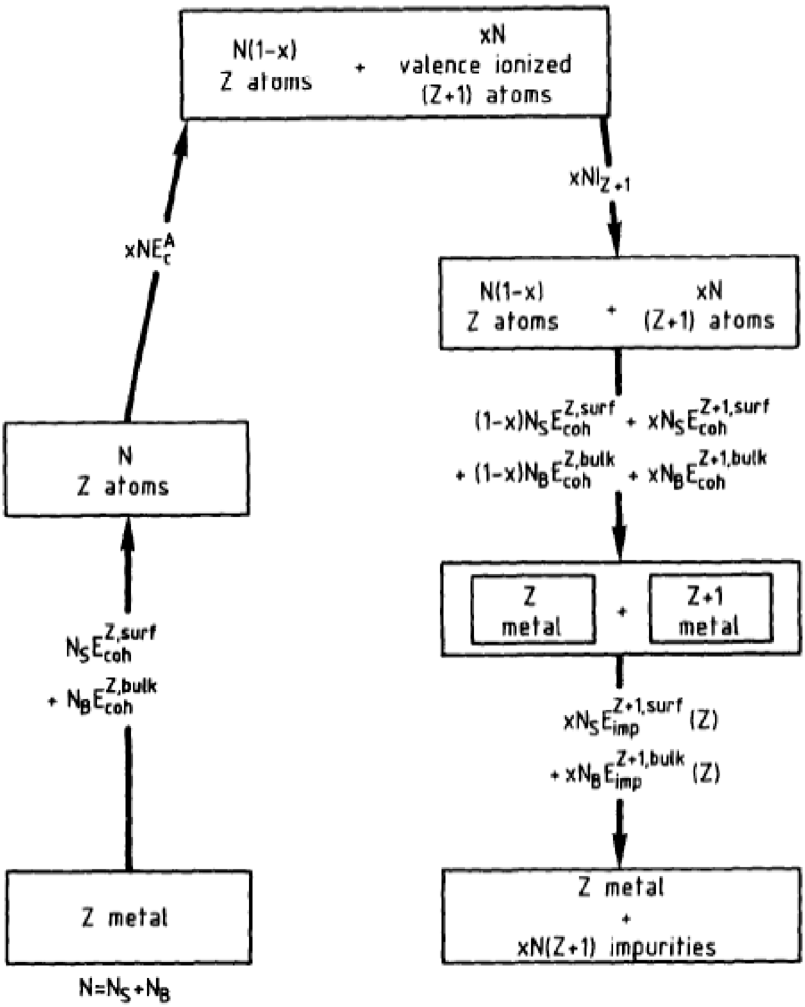

Fig. 3.3.6. *Born-Haber cycle for the core level binding energy shifts of clean surfaces [120].*

The above models can be extended to adsorbate-covered surfaces using modifications described in ref. [120].

In the case of Si(100), limited resolution complicated the identification of the SCLS components in the 2*p* spectra prior to the high resolution work by Landemark *et al.* [45]. In this study, four SCLS components with shifts of +0.49, +0.21, -0.06, and –0.22 eV relative to the bulk component were resolved for the c(4×2) structure and closely similar values were found for the (2×1) structure (Fig. 3.3.7, left panel). The components at +0.49 eV and -0.06 eV were assigned to the up- and down-atoms of the Si dimer, respectively, and the peak at –0.22 eV was assigned to second layer Si atoms whereas the origin of the peak at +0.21 remained unresolved. Such results could not be interpreted within the initial state theory, which predicted remarkably different shifts, as seen in Fig. 3.3.7 right panel. Pehlke and Scheffler [122] introduced the final state theory and interpreted the shifts in terms of core hole screening. An enhanced screening was observed at the surface and, due to the particular electronic structure of the Si(100) surface (with filled dangling bond state localized at the up-atom and empty dangling bond states localized at the down-atom), the hole localized in the down-atoms has a stronger screening effect than the hole localized in the up-atoms [122].

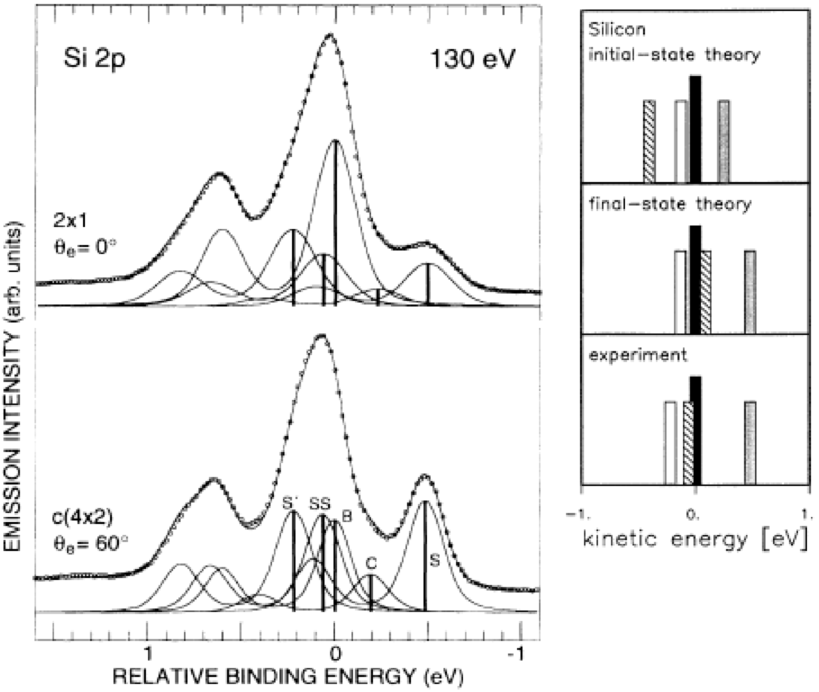

Fig. 3.3.7. *Left panel: First high resolution core level spectra of Si(100) by Landemark et al. where four surface components were resolved. The components denoted by S, SS, and S' are assigned to the up-atoms, down-atoms, and second layer atoms, respectively. From ref. [45]. Right panel: Calculated SCLSs of Si(100) by initial state (top) and final state (middle) theories, and experimental values taken from the left panel (bottom). Black bar is bulk component B; grey, hatched, and white bars correspond to up-atom, down-atom, and second layer atom components, respectively. From ref. [122].*

The energy reference level

In experiments, conducting samples (also semiconductors or conducting samples with a thin insulating overlayer) and the spectrometer are brought to electric contact so that their Fermi energies are at the same level; thus the work function in eq. (3.3.1) is the spectrometer work function φ_{sp} as illustrated in Fig. 3.3.8. For metals, E_F can be found experimentally as it is equivalent to the maximum kinetic energy at which electron emission occurs. Thus φ_{sp} can be determined and the zero of the E_B scale can be located at E_F. The value of φ_{sp} remains constant for a particular spectrometer under unchanged environment. In semiconductors, E_F lies in the band gap and cannot be directly observed, however, the position of E_F in the spectrum can be defined using a metal reference sample. Furthermore, at semiconductor surfaces band bending occurs due to the doping and surface states in the band gap, giving an additional contribution to the energy reference problem [116]. Insulating samples experience positive charging due to electron emission, which is usually compensated by a flow of extra electrons. Finding the correct reference level for measured E_B for insulators requires knowledge of the sample work function, φ_s, and the energy of flooding electrons.

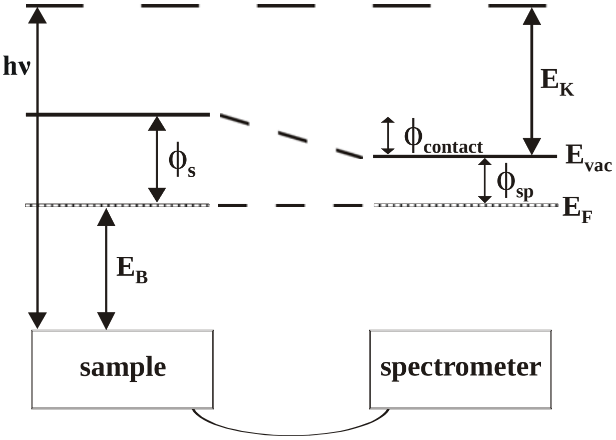

Fig. 3.3.8. *Energy level diagram for the photoemission process. The sample and spectrometer are electrically connected so that their Fermi energy levels (E_F) coincide. If the work functions of the sample and spectrometer (φ_s and φ_{sp}, respectively) differ, a contact potential $\varphi_{contact}$ is formed. The measured kinetic photoelectron energies (E_K) are independent of the sample work function.*

Peak intensity

The intensity of a photoelectron peak depends on the cross section (σ) of the photoelectric effect, which is the transition probability from the initial state ψ_i to the final state ψ_f [90]. The photon beam can be treated as a small perturbation H'

$$H' = \frac{e}{2mc}(\boldsymbol{A}\cdot\boldsymbol{p} + \boldsymbol{p}\cdot\boldsymbol{A}), \qquad (3.3.11)$$

where $\boldsymbol{p} = -i\hbar\nabla$ is the momentum operator and $\boldsymbol{A}$ is the vector potential of the incident electromagnetic wave:

$$\boldsymbol{A}(\boldsymbol{r},t) = \boldsymbol{e}A_0 \exp[i(\boldsymbol{k}\cdot\boldsymbol{r} - 2\pi\nu t)], \qquad (3.3.12)$$

where $\boldsymbol{e}$ is a unit vector in the direction of the light polarization, A_0 the amplitude, $\boldsymbol{k}$ the wave vector with $k = 2\pi/\lambda$ and λ = the wavelength. The transition probability is then proportional to the squared matrix element (summed over N electrons):

$$\left|M_{if}\right|^2 = \hbar^2 A_0{}^2 \left| < \psi_f \left| \sum_{i=1}^{N} \exp(i\boldsymbol{k}\cdot\boldsymbol{r}) e\cdot\nabla_i \right| \psi_i > \right|^2. \qquad (3.3.13)$$

If we further assume that λ is large compared to the atomic dimensions, eq. (3.3.13) simplifies to the "dipole approximation"

$$\left|M_{if}\right|^2 = \hbar^2 A_0{}^2 \sum_{if} \left| \boldsymbol{e}\cdot < \psi_f \left| \sum_{i=1} \nabla_i \right| \psi_i > \right|^2. \qquad (3.3.14)$$

The approximation which is most commonly used to calculate the matrix element is derived from the one-electron picture and from the assumption that the primary excitation is rapid with respect to the relaxation of the remaining electrons (the "sudden approximation").

Line shape

The width of a photoelectron peak is determined by the lifetime of the core hole, the instrumental resolution, and the presence of unresolved satellite structures [89, 115, 117]. The line width is expressed in eV as FWHM, the full width at half maximum of the peak. In the spectrum there is always a background due to the electrons that have lost their energy in inelastic scattering.

The intrinsic line width due to the finite core hole lifetime is given by the Heisenberg's uncertainty relation

$$\Gamma = \frac{h}{\tau}, \tag{3.3.15}$$

where Γ is the width, h is Planck's constant, and τ is the core hole lifetime. Instrumental contribution is caused by energy spread of the incident photon beam and the resolution of the analyzer. The line shape due to lifetime broadening is Lorentzian and that due to instrumental broadening is Gaussian [115]. Satellite features can arise from coupling of the hole to the vibrational states, multiplet splitting, or shake-up satellites. In metals, the outcoming photoelectron may transfer part of its kinetic energy to excite a valence electron to the conduction band, which induces an asymmetric tail to the higher BE side of the peak. The line shape for semiconductors can be considered symmetric.

3.3.3. Spectral line shape analysis

In this work, the peak fitting procedure of Si and RE-metal photoemission spectra was done using the Origin 6.1 program and Voigt lineshape, which is a convolution of Lorentzian and Gaussian functions. The inelastic background was removed using the Shirley method [123]. Metallic samples often exhibit asymmetric line shape that cannot be fitted by a symmetric Voigt function. Doniah-Sunjic –lineshape, with a singularity parameter α related to the amount of asymmetry can be applied to metallic samples. Such a fitting was also tested in the case of RE-metals, but the value of the α-parameter was found to be close to zero, ie, the line shape was found to be symmetric.

Several physical constraints were taken into account to restrict the number of free parameters and to obtain reliable fitting results:

- The Lorentzian width (LW) was fixed.
- Spin-orbit splitting was kept constant for each line (e.g., for all Si 2*p* components throughout a series of spectra for various RE –metal coverages).
- The branching ratio of the spin-orbit-split components was expected to have the statistical value (e.g., 2:1 for $2p_{3/2}$ and $2p_{1/2}$ components). However, small variations were allowed.
- The number of components was chosen to be as small as possible in the limit of reasonable fit.

- The Gaussian width (GW) and energy shifts (ie, the SCLSs) of different surface components were variable parameters. For an individual component, the GW and SCLS were kept constant throughout the fitting. Surface-related components had slightly higher GWs than the bulk component.

The fitting parameters and atomic origins of components in the Si 2*p* spectra of the clean Si(100) surface are well established, e.g. the in high-resolution photoemission study by Landemark *et al.* [45]. Therefore, by first fitting the spectra from a clean Si(100) surface and comparing the obtained parameters with those in the literature, the reliability of the procedure could be confirmed.

3.4. Other methods

Auger electron spectroscopy (AES), thermal desorption spectroscopy (TDS), and work function change ($\Delta\varphi$) measurements have also been applied in the study of the flat Yb/Si(100) interface [Paper I]. A short description of these methods is given here.

The initiation of an Auger process is the ionization of a core level. The excitation is typically carried out by electrons with an energy of 1 – 10 keV, or by photons in the soft X-ray regime [115]. An electron falling from an outer level fills the initial core hole and the released energy is transferred to a third electron, an Auger electron, which is emitted from the atom. An alternative decay mechanism is X-ray fluorescence where the excess energy is given up to an outgoing photon. In Fig. 3.4.1 the Auger process is illustrated using the K, L_1, and $L_{2,3}$ levels, ie by the $KL_1L_{2,3}$ transition (using conventional X-ray notation). An electron from L_1 shell fills the initial core hole in the K shell and an electron from the $L_{2,3}$ shell is ejected. The energy of the Auger electron is

$$E_{KL_1L_{2,3}} = E_K - E_{L_1} - E^*_{L_{2,3}}, \tag{3.4.1}$$

where E_i are the binding energies of the ith atomic energy levels. The star in $E^*_{L_{2,3}}$ denotes that it is not the ground state of level $L_{2,3}$, but the binding energy of $L_{2,3}$ level in the presence of a hole in level L_1.

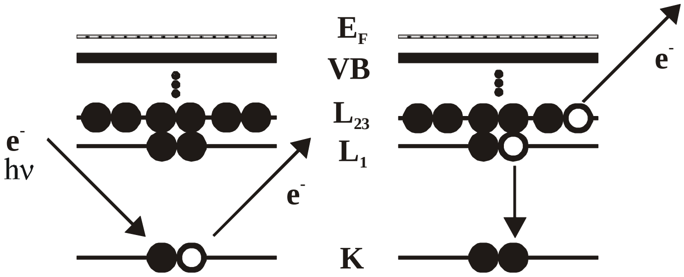

Fig. 3.4.1. *Illustration of the KLL Auger process. Left: The initial core hole in the K shell can be created by electron or photon excitation. Right: An electron from the L shell fills the initial hole and the excess energy is transferred to another L electron, which is emitted and detected as an Auger electron.*

Auger electron spectroscopy is based on measuring the kinetic energy of the emitted electron, which is unique to each atom and independent of the mechanism used to create the initial core hole, as seen from equation (3.4.1). Thus AES provides elemental identification, except for H and He. When recording the spectra in the energy range of 0 – 2 keV, the electron escape depth λ in solids is few nanometers, ie, AES is surface sensitive (see Fig. 3.3.5. for mean free path). The incident electron beam penetrates much deeper than the escape depth of electrons into the solid and is able to ionize atoms in the depth of 1 – 2 µm, as shown schematically in Fig. 3.4.2. This induces high background to the Auger spectrum; therefore, quantitative analysis of the Auger spectra is complicated. In practice, the Auger spectra are often recorded in the electronically differentiated mode: d*N*(*E*)/d*E* as a function of *E*. The Auger peak heights can be used as a measure of relative surface concentrations if experimental conditions are otherwise held constant [90].

In combination with ion sputtering, AES is often applied to depth profiling. Scanning Auger microscopy (SAM) takes advantage of the high spatial resolution of AES.

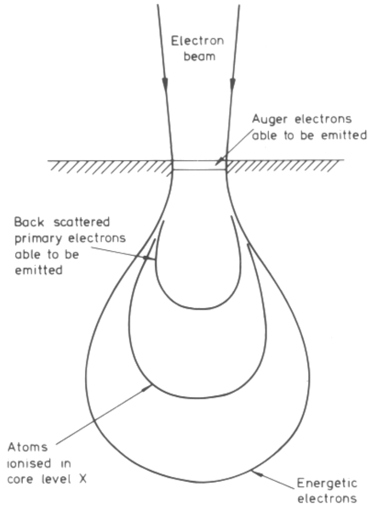

Fig. 3.4.2. *Schematic presentation of the electron scattering in AES [115].*

In thermal desorption spectroscopy (TDS), also known as temperature programmed desorption (TPD), the sample is heated with a controlled temperature program and the species desorbing from the sample are measured, e.g. by mass spectrometry. Adsorbed particles from inequivalent adsorption sites will desorb at different temperatures, therefore the number of features in the TD spectrum gives a suggestion of the number of possible adsorption sites on the surface. The shape of TD peaks is characteristics of reaction order, *n*, which in turn gives qualitative information of the reaction kinetics. The desorption rate r_{des} can be expressed by the Polanyi-Wigner –equation, which can be written as

$$r_{des} = \frac{d\theta}{dT} = -\frac{\nu(\theta,T)\theta^{n}}{\beta}\exp\left[\frac{-E_{des}}{RT}\right], \qquad (3.4.2)$$

where $\beta = \frac{dT}{dt}$ is the temperature 'ramp' (heating rate), T the temperature, t the time, θ the adsorbate coverage, v the pre-exponential (frequency) factor, E_{des} the activation energy of desorption, and R the molar gas constant. Several methods have been used to evaluate the desorption parameters in eq. (3.4.2). Correct results are obtained by the so-called complete method; approximate methods like leading edge analysis, the Redhead method, Arrhenius plots, and heating rate variations are easy to apply and acceptably accurate as long as their limitations are properly taken into account [124].

The electronic charge density near the surface of a crystal tunnels into the vacuum region, which creates an electrostatic dipole layer at the surface. The surface layer, the so-called double layer, determines the work function. Adsorption of atoms or molecules causes charge redistribution in the double layer, and the value of the work function is strongly dependent on the coverage and atomic arrangement of the adsorbate. For semiconducting substrates, interaction with adsorbates can cause a shift of the Fermi level that gives an additional contribution to the work function. The work-function change can be measured, for example, by the contact potential method.

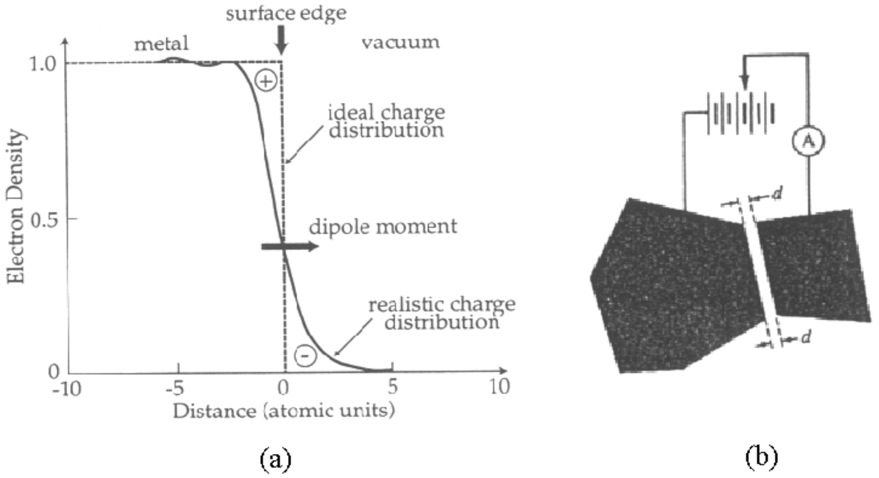

Fig. 3.4.4. *(a) Electron-density distribution at the edge of a metal surface [1]. (b) An illustration of the contact potential measurement: When the distance d between two parallel plates is varied, the charge density on the surfaces changes, but the contact potential remains unchanged, which induces a current flow between the plates. By applying an external potential bias and adjusting it so that no current flows, the external bias cancels exactly the contact potential. From ref. [125].*

4. Experiments

The experimental techniques described in the previous section should be operated in an ultra high vacuum (UHV) environment in order to reach the required level of surface specificity. One reason is due to the techniques themselves: in electron spectroscopy and LEED, the mean free path of the electrons should be long enough to prevent a loss of electrons due to collisions with residual gas molecules. Secondly, the most stringent requirement on the vacuum conditions arises from the need for a clean and stable surface. When working with the extreme surface sensitivity any contamination or instability has to be avoided.

4.1. Experimental set-ups

The experiments were performed in The Laboratory of Materials Physics at University of Turku, Finland (LEED, STM/STS), and in The MAX-laboratory at Lund University, Sweden (LEED, SR-PES), and in The A. F. Ioffe Physico-Technical Institute in St. Petersburg, Russia (AES, TDS, $\Delta\varphi$). The experimental set-ups used in Turku and Lund, and described below, represent typical systems where the requisite UHV pressure regime is achieved by a combination of turbomolecular pumps, ion pumps, and titanium sublimation pumps. Inside the systems, a sample can be transferred between the different chambers without breaking the UHV conditions.

In the Turku laboratory, the experimental system consists of a loading chamber, preparation chamber, analyzing chamber including STM-unit, and KRIPES-chamber (Fig. 4.2.1). Several experimental techniques are available: STM/STS, AFM, LEED, X-ray photoemission spectroscopy (XPS), ultraviolet spectroscopy (UPS), k-resolved inverse photoemission spectroscopy (KRIPES), and TDS. Several procedures can be applied to samples in UHV, e.g. heating, ion sputtering, and deposition of different materials.

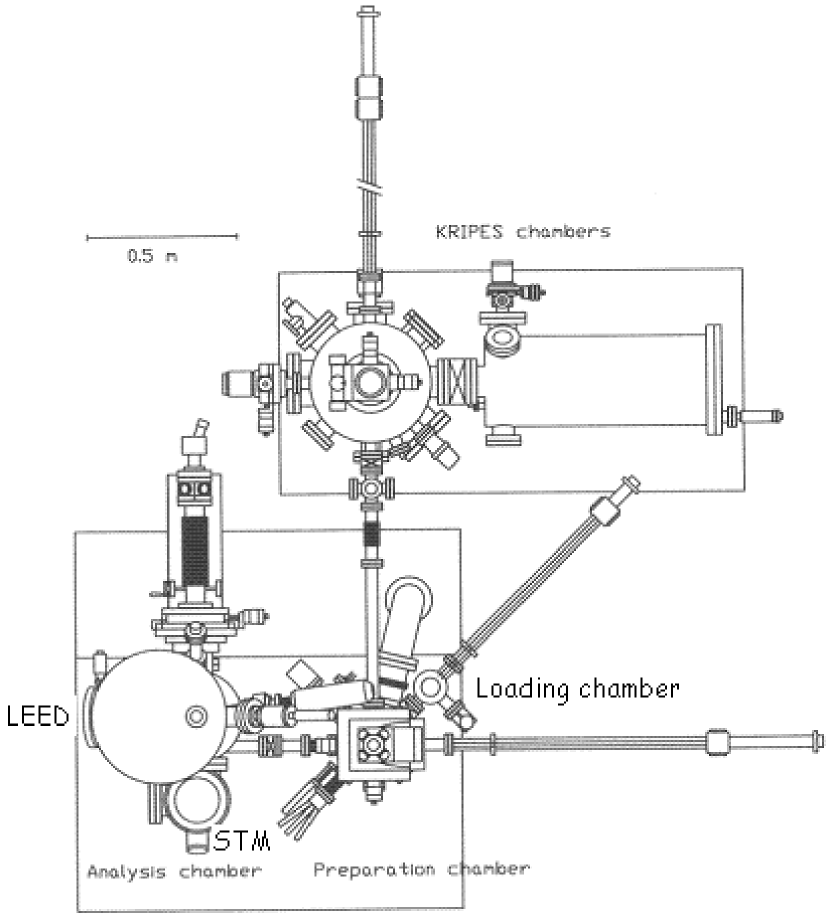

Fig.4.2.1. *Schematic illustration of the experimental set-up in Turku laboratory [126].*

The MAX-laboratory is a synchrotron radiation facility where our experiments were carried out at beamline 33 (BL33) in the MAX I storage ring. Technical details can be found in Table I. The end station, shown in Fig. 4.2.2, has a loading chamber (Air-lock), preparation chamber, sample transfer chamber, and analyzing chamber for angle resolved photoemission measurements (ARUPS chamber). The photon energy range (15 – 200 eV) is suitable for valence band measurements as well as Si2p core-level and RE-metal 4f states studies.

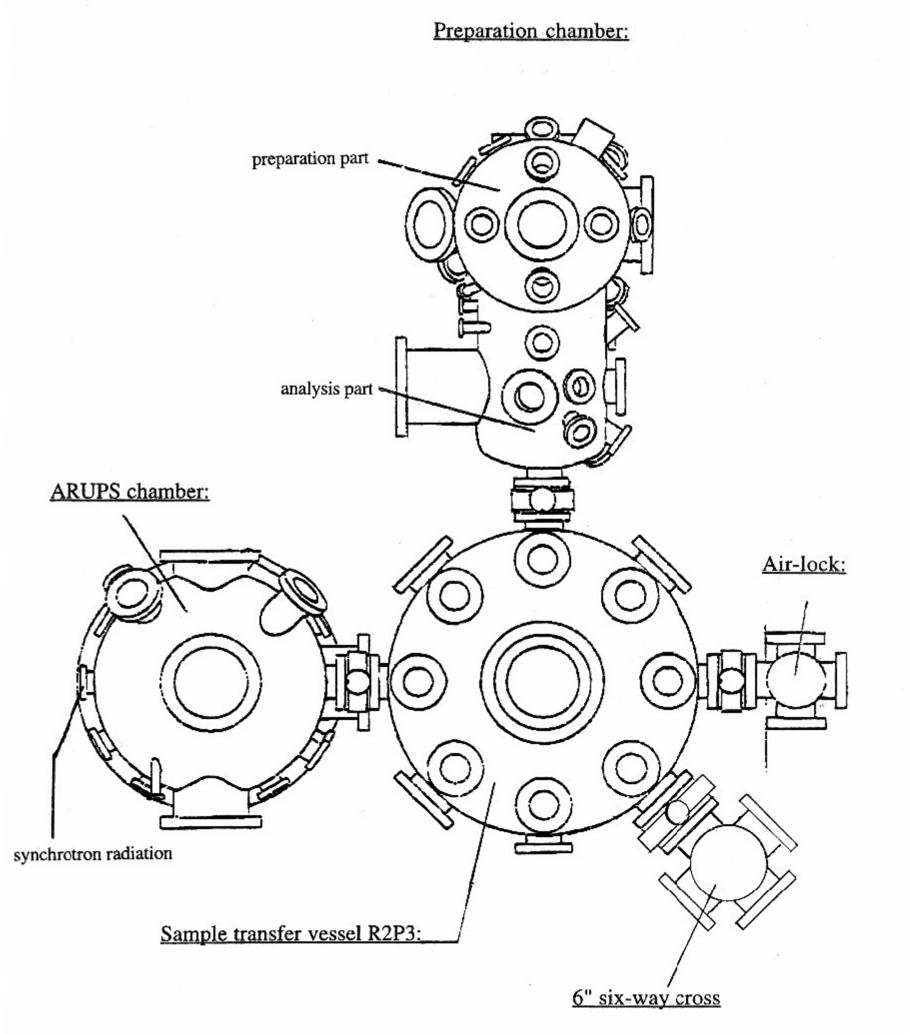

Fig.4.2.2. *Schematic illustration of the end station at beamline 33 in MAX-lab [127].*

***Table I.** Technical parameters of beamline 33 in the MAX I storage ring of MAX-lab [127].*

TECHNICAL DATA:

Source:		Bending magnet, 12 mrad.
Pre-focusing optics:		Vertically and horizontally focusing spherical mirrors.
Monochromator:		5.5 - 5.8 m, 162 deg. SGM with three gratings (300 l/mm, 700 l/mm and 1500 l/mm) and a movable exit slit.
Energy range:		15 - 200 eV.
Energy resolution:		$E/dE = 4x10^3 - 1.5x10^4$.
Higher order suppression optics:		Two plane mirrors with variable angle of incidence and C, Al and Si coatings.
Re-focusing optics:		Toroidal mirror.
Photon flux on sample:		10^{10} - 10^{11} ph/s.
Spot size on sample:		2 x 1 mm^2.
Experimental station:		This is a commercial surface science system from VG Microtec. It consists of a preparation chamber, a sample storage chamber, a sample introduction chamber and an analyzer chamber. The preparation chamber is equipped with LEED, ion sputtering gun, gas-inlet system and a number of optional ports for user owned sample preparation accessories. The analyzer chamber is equipped with a goniometer mounted angular resolved electron energy analyzer (ARUPS10) specially designed to have an electronically variable angular resolution (±0.4 to ±2.0 deg.).

4.2. Sample preparation

Samples were cut from mirror-polished n-type Si(100) wafers doped by P (1 – 2 Ω cm). The vicinal wafers were miscut by 4° from the (100) plane towards the [011] direction. The size of the sample pieces was 3 – 5 mm × 12 mm. The samples were rinsed with ethanol and de-ionized water before inserting into the UHV. In the UHV, the samples were degassed at 600 °C for several hours, usually over night. In order to remove all contaminants and obtain a well-ordered surface, the samples were treated using sophisticated flashing procedures. The details of flashing depend on whether the sample is flat or vicinal. Flat samples were flashed a few times at 1150 °C for 30 – 60 s each time, then annealed at 980 °C for 10 min, and finally cooled slowly to room temperature. Preparation of a good vicinal Si(100) surface is not straightforward but requires careful temperature and pressure control. Flashing of vicinal samples at 1150 – 1200 °C was repeated until the total time at high temperature and low pressure was at least two minutes. After the last flash, the temperature was quickly decreased to 900 °C and kept there for 5 minutes. The procedure was finished by gradual cooling to RT at a rate of 20 °C/min. The temperatures were measured by infrared pyrometers with an estimated accuracy of ± 20 °C.

The deposition of adsorbate materials Eu and Yb was performed using homemade W-coil evaporators. The fluxes of Eu and Yb were measured by a quartz-crystal microbalance thickness monitor. In some experiments, an independent calibration using a separate Si(111) sample was applied. The phase diagrams for the Eu/Si(111) and Yb/Si(111) systems as a function of metal coverage are well-defined from previous experiments [Paper VIII, Paper XII, 128, 129]. The deposition rate was 0.3 – 1.0 monolayers (ML)/min. One monolayer is defined as the number of atoms on a bulk-truncated Si(100) surface, that is, 6.78×10^{14} atoms/cm^2. It corresponds to a thickness of 3.3 Å and 2.8 Å for Eu and Yb, respectively.

The formation of well-ordered RE/Si surface reconstructions does not take place at room temperature; therefore annealing is required. The annealing temperature should be high enough to stabilize the ordered surface phases but below the temperature where desorption of adsorbate starts. There are two alternative procedures, either one can perform the evaporation at RT and subsequently anneal the sample, or keep the Si substrate at an elevated temperature during deposition. The former method was applied in our studies except for vicinal Yb/Si(100), where both techniques were used. The annealing temperature was 600 °C for Eu/Si surfaces, 530 °C for flat Yb/Si surfaces, and 540 – 640 °C for vicinal Yb/Si systems. The time required for the subsequent annealing varied between 3 and 10 minutes.

It should be mentioned that the same sample preparation procedure and similar devices for measuring the temperatures and evaporation fluxes, as well as LEED, were available in the Turku laboratory and MAX-laboratory. In addition, the base pressure in both UHV systems was in the same regime, that is 2×10^{-10} mbar or below. Thus we can assume that the RE/Si surfaces prepared in these laboratories have been identical.

5. RE metal induced reconstructions on Si(100)

5.1. An introduction to rare earth metals on silicon

The rare earth (RE) series in the atomic data table starts from lanthanum (atomic number 57) and ends to lutenium (atomic number 71) and is characterized by a progressive filling of the 4*f* subshell. When attached to Si surfaces, the RE metals, as well as the related IIIA metals Sc and Y, react easily and form silicides. The study of RE metal silicides began in the early 1980's and it was soon noticed that they form a distinct class among the other transition metal silicides [130]. Important properties, which make RE silicides attractive for various applications, are a low temperature of formation, linear growth rate with time, good electrical and thermal conductivity, and the lowest known Schottky barrier heights on *n*-type Si [131, 132]. Interest has, in particular, been focused on the structural properties of the RE-Si interfaces promoted by the formation of epitaxially ordered RE silicides, as first evidenced on Si(111) [133], and furthermore, by observation of 2D epitaxial growth [134].

The outer electronic configuration of RE metals is determined by delocalised 6*s* and 5*d* electrons, which form a hybridized conduction band in the solid state. The 4*f* electrons are highly localized and do not directly participate in covalent bonding. All of the RE bulk metals are trivalent except for Yb and Eu, which are divalent [135]. In compounds and alloys the valency of RE metals is dependent on the chemical environment; three types of configurations are possible: (i) an integer valency of 2 or 3; (ii) a multiple valency of 2 and 3 where the RE atoms at different lattice sites have the valency of 2 for one type of site and the valency of 3 for the other type of site; (iii) a dynamical intermediate (mixed) valency state in which a given electron can be found at a given time either localized in the 4*f* subshell or delocalized in the conduction band, thus leading to a noninteger valency number between 2 and 3. Such a fluctuating valency occurs for Ce, Sm, Eu, Tm and Yb [135], providing these elements with the capability to change their valency as a function of the chemical environment. The electronic configuration of the 4*f* subshell, which can be obtained from 4*f* photoemission spectra, can be used to determine the chemical state of these elements in a given environment.

In rare earth silicides most of the RE atoms are trivalent or exhibit multiple valency. However, Eu is divalent [136] whereas Yb can be either divalent or have a mixed valency [137].

The RE silicides are formed in three major stoichiometries: in the metal rich forms as RE_5Si_3 and RE_5Si_4 silicides, as monosilicides RESi, and as disilicides of varying composition $RESi_{(2-x)}$, where x is between 0 and 0.3. The interface formation is a multistep process where the metal-rich silicide-type phases are likely to be formed at the reacted room-temperature interfaces and the transition to Si-rich disilicide-type phases occurs upon thermal activation, ie annealing the reacted surface at an elevated temperature or via a reaction directly on the Si surface maintained at an elevated temperature. The disilicides have been of most interest to researchers. Especially interesting is the $RESi_{1.7}$ silicide with AlB_2 crystal structure forming epitaxial reconstructions on the Si(100) and Si(111) surfaces.

Ordered RE/Si phases were first found on Si(111), as reviewed in Refs. [131, 132, 138]. It was suggested in [139] that only amorphous silicide phases would occur on the Si(100) surface. However, interest soon turned towards the technologically more important Si(100) for the following reasons: ordered two-dimensional Sm-induced reconstructions on Si(100) were observed in the submonolayer coverage regime [140 – 142], a possibility to form epitaxial RE-silicides also on Si(100) was introduced in the study of the Gd/Si interface [143], and epitaxial growth was reported for Lu [144], Er [145] and Y [146]. Finally, 1D RESi wires were discovered on Si(100); they were first observed for Dy [147] and later for Er [148].

5.2. Two dimensional RE metal reconstructions on Si(100)

In general, the growth of RE metals on Si can be considered in terms of the Stranski-Krastanov growth mode. A two dimensional layer wets the surface prior to 3D growth starting as islands or wires on top of the wetting layer which persists on the substrate. However, the growth is not purely Stranski-Krastanov type since the 3D structures can appear at such low coverages that areas of uncovered Si surface still exist [149]. There are also reports of 3D growth on a bare Si substrate for Ho [150], Dy [151] and Er [148, 152]. The role of 2D reconstructions is significant being the first stage in the growth process, and a large variety of ordered phases has been observed for the different RE metals on Si(100). Some general trends can be found among the 2D structures. A reconstruction with the 2×3 periodicity is formed by Nd [153], Sm [142, 154], Eu [Papers II – IV], Er [155] and Yb [Paper I, Paper II, 153,]. In the cases of Nd and Yb, the 2×3 type structure can also appear as a modified 2×4 structure [Paper I, Paper II, 153]. Another subgroup consists of Gd [156, 157], Dy [156, 158, 159], and Ho [150], which form a 2×4 reconstruction followed by one which is 2×7. Within this group the 2D structure is closely related to the formation of nanowires. That is, the NW width is determined by the 2D reconstruction.

Scanning tunneling microscopy images of the low coverage 2×3 and 2×4 structures have revealed a construction formed by bright and dim maxima arranged in bright-dim pairs and in units of bright-dim-bright or dim-bright-dim for the 2×3 and 2×4 structures, respectively. The positions of STM maxima with respect to the Si substrate correspond to the original positions of Si dimers for Yb, Nd, Dy, Gd, and Ho [150, 153, 156, 158] whereas for 2×3-Sm the registry of maxima with respect to the Si dimers is out of phase [154]. However, the number of metal atoms per STM maxima is under debate; for Yb, Nd, Dy, and Gd it has been suggested that the number of metal atoms is equal to the number of STM maxima [153, 156, 158], but for Ho 1.5 atoms per a 2×4 unit cell with the three maxima were proposed [150]. For Gd, Dy, and Ho, the 2×7 structure contains the former 2×4 structure as a subunit [150, 156]. For Yb and Nd the 2×3/2×4 phase is followed by a 2×6 structure [Paper I, 153].

In addition other 2D phases have been reported, for example: c(4×2), 4×2, 5×2 and c(5×4) for Er [155, 160], 2×1-“wavy” for Eu [Paper III] and Sm [154], 3×2 for Sm [154], 2×8 for Gd [157], 1×3 for Yb and Nd [153], and in addition to 1×3, also 1×5 and 1×9 for Yb [Paper V].

5.3. Nanowire formation and the growth of 3D RE-silicides on Si(100)

Three-dimensional silicide growth starts as isolated islands, which coalesce as the amount of RE metal increases, forming a continuous film. For example, silicide islands with rectangular shape have been reported for Dy [161, 162], Nd [153], Yb [153] and Sm [154]. Transmission electron microscopy (TEM) studies of continuous silicide films in the thickness regime of tens of nanometers have revealed the growth of epitaxial RESi$_{2-x}$ for Yb [163], Dy [164], Er and Tb [165].

In heteroepitaxial growth, the difference in lattice constants of the substrate and the growing material play a crucial role. A deviation from the perfect lattice match induces strain between the constituents. Anisotropy in the strain leads to anisotropic growth; the orientation where the lattice mismatch is small is the most favourable direction of growth whereas growth is diminished in the direction with a large mismatch. Therefore, the RE silicides exhibiting a good lattice match in one direction and a variety of positive and negative lattice mismatches in the orthogonal direction, may also form 1D nanowires on the Si(100) substrate.

Lattice mismatch model

The lattice-mismatch model assumes that the RE nanowires have crystallized in a hexagonal disilicide RESi$_{2-x}$ lattice structure where the self assembly arises from a small lattice mismatch of the $[11\bar{2}0]$ silicide axis (the *a* axis) along one of the Si[011] directions and a large mismatch of the [0001] silicide axis (the *c* axis) along the other Si[011] direction [148, 149]. The RESi$_{2-x}$ structure is an AlB$_2$ type crystal where planes of the RE metal and Si alternate along the [0001] axis. Vacancies are introduced in the Si plane in order to relieve the strain [166]. Lattice constants of the RESi$_{2-x}$ structure for several RE silicides and their mismatch to the Si(100) lattice are presented in Table II. Figure 5.3.1. shows the hexagonal unit cell and its relative orientation on the Si(100) substrate.

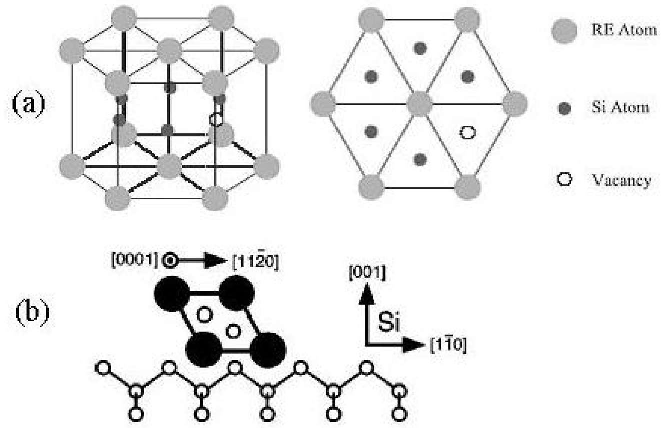

Fig. 5.3.1. *a) A unit cell of RESi$_{1.67}$, which is the hexagonal AlB$_2$ structure with one of the six Si atoms missing [167]. b) A schematic illustration of the relative orientation of the silicide and the Si substrate [149].*

Table II. *Lattice constants of some hexagonal RE silicides. Mismatch as compared to the Si(100) surface with a lattice constant of 3.84 Å, is expressed as a percentage. From ref. [151].*

Lattice mismatch between hexagonal phase of various rare earth silicides and Si(100)				
Rare earth	*a* (Å)	(%)	*c* (Å)	(%)
$ScSi_{1.7}$	3.66	(–4.69)	3.87	(+0.78)
YSi_2 (hexagonal)	3.842	(+0.05)	4.144	(+7.92)
Sm_3Si_5 (hexagonal)	3.90	(+1.64)	4.21	(+9.64)
$GdSi_2$ (hexagonal)	3.877	(+0.96)	4.172	(+8.65)
$DySi_2$ (hexagonal)	3.831	(–0.23)	4.121	(+7.32)
$HoSi_2$ (hexagonal)	3.816	(–0.63)	4.107	(+6.95)
$ErSi_{2-x}$ (hexagonal)	3.79	(–1.30)	4.09	(+6.51)
$YbSi_2$	3.784	(–1.46)	4.098	(+6.71)

Nanowires

Nanowires with the $RESi_{2-x}$ lattice on the Si(100) have been reported for Er [148, 168 – 179], Sm [178, 179], Dy [147, 149, 159, 162, 177 – 181], Gd [177 – 179, 181 – 183], Ho [149, 150], Yb [Paper VI, Paper VII], and Ce [184]. For Gd another type of NW with an orthorhombic structure has been observed [183]. The formation of NWs depends on the annealing time and temperature and the metal coverage; formation of NWs usually occurs at low coverage at ~ 600 °C after a short annealing time, whereas higher temperature or prolonged annealing, as well as a higher coverage, leads to the formation of 3D islands [159, 169]. It has been suggested that the hexagonal phase is related to the NWs whereas tetragonal or orthorhombic phases correspond to 3D islands [170, 173, 181].

On the anisotropic Si(100) surface the RE nanowires have a preferential orientation, that is, they tend to grow perpendicular to the Si dimer rows [148]. The growing nanowires interact with the steps on the substrate in such a way that they never cross a step edge. As the end of a NW approaches a step edge, it causes a "snow-plow" effect where the terrace retreats from the wire, leading to step bunching [148, 149, 159, 169, 175, 177]. On the double domain Si(100) surface, growth is limited either when the advancing NW meets another orthogonal NW, since the NWs never cross one another, or when the retreating step bunch in front of the NW has become too high to penetrate [179, 182].

The vicinal Si(100) surface offers a growth template with only one preferential orientation for the NW formation, ie, that parallel to the step edges. Furthermore, a probability of the growing NW meeting limiting obstacles, such as step bunches, kinks or another NW running in an orthogonal direction, is considerably diminished. A few studies of RE nanowires on the vicinal Si(100) substrate have been reported [171, 172, 176, 178, 179, 181, 184]. In these studies, the single orientation of the NWs was confirmed and it was found that high aspect ratios of the order of 1000 could be achieved. The single nanowires usually form bundles. On the vicinal substrate the bundle width has shown to be dependent on the original terrace width for Gd, Er, Dy and Sm [179].

Electronic properties of the NWs have been studied by scanning tunneling spectroscopy (STS), which measures the local electronic structure. For Dy [149], Ho [149, 150] and Gd [179, 182] metallic behaviour was found for NWs while the surrounding 2D layer was found to be non-metallic.

5.4. Results and discussion of papers

In the present study, Eu and Yb induced surface reconstructions on flat and vicinal Si(100) substrates have been investigated. Among the RE metals, Eu and Yb are peculiar since they are divalent, having a stable electronic configuration with half filled or completely filled 4*f* subshells, respectively. They are expected to be less reactive than the other RE's, and therefore the onset of silicide formation in these RE/Si(100) systems is expected to occur at a higher coverage than for the other RE's, thus enabling the study of 2D reconstructions on the surface without the presence of the silicide phase. The two stages of RE/Si(100) interface formation were studied. The 2D layer formation in the submonolayer RE metal coverage regime was examined for both the metals. To study the silicide formation stage, Yb was chosen, as the Yb silicide has an ordered AlB_2 structure.

Papers I – IV

The two-dimensional adsorbed layer was examined in Papers I – IV. In Paper I, the formation of 2×3 and 2×6-Yb reconstructions on a flat Si(100) substrate were studied using AES, TDS, $\Delta\varphi$, LEED, and STM. In Paper II, we studied Eu- and Yb-induced reconstructions on the vicinal Si(100) substrate at 0.1 – 0.3 ML using LEED, STM, and PES. In Paper III, Eu-induced 2×3 and so-called "wavy" structures and a double- to single-domain transition on the slightly miscut Eu/Si(100) surface at 0.4 ML were studied by LEED and STM. The formation of the 2×3-Eu reconstruction was examined in details by LEED, STM, STS, and PES in Paper IV.

The STM images from both Eu/Si and Yb/Si surfaces were strongly dependent on the applied bias voltage. The Eu/Si images were also affected by the tunneling current . Thus the STM images represent not only the geometric structure but the electronic effects as well. Several possible models were considered for the 2×3 type reconstruction common to both adsorbates. By analysing the results obtained by experimental methods many of the proposed models could be ruled out, and finally the most plausible atomic models were found. The detailed atomic structures of 2×3 units were found to be somewhat different for Eu/Si and Yb/Si; moreover, the suggested models differ from those proposed earlier in the literature for other 2×3 phases. It can be concluded that the adsorbate atoms have a crucial role in the formation of metal-induced 2×3 reconstructions on the Si(100) surface. The atomic models for the Yb and

Eu induced Si(100)2×3 phases are shown in Figs. 5.4.1. and 5.4.2., respectively. For Yb/Si, it is suggested that adsorption takes place in valley sites on the Si surface exhibiting unreconstructed 1×1 ordering. For Eu/Si, it is suggested that adsorption takes place in pedestal and valley sites with the underlying surface exhibiting a 1×3 reconstruction formed by rows of Si dimers and monomers running in a direction perpendicular to the original dimer row direction. Such model was found to be in agreement with the STM images and with the STS and SR-PES results shown in Figure 5.4.3.

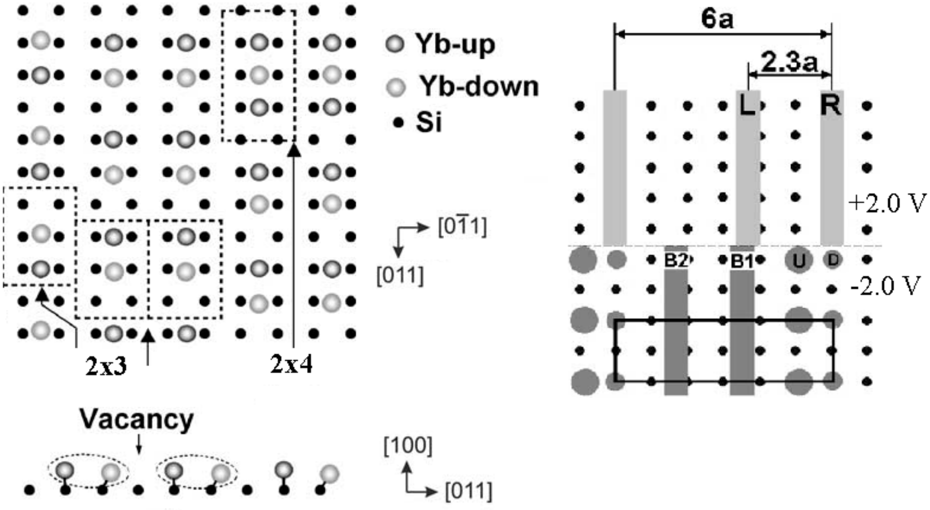

(a) (b)

Fig. 5.4.1. *Models for Yb-induced reconstructions on Si(100). (a) The 2×3 unit is composed of one Yb-up atom, one Yb-down atom, and one vacancy whereas in the 2×4 unit cell there are three Yb atoms ordered either by up-down-up or down-up-down. (b) Schematic model of the complicated 2×6 structure where the features, which were observed in filled state (-2.0 V) and empty state (+2.0V) STM images, are indicated. From Paper I.*

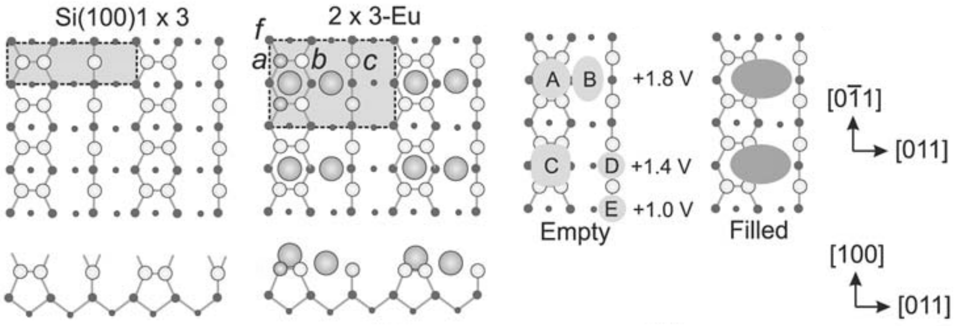

(a) (b) (c)

Fig. 5.4.2. *Atomic model for the Eu-induced 2×3 reconstruction on Si(100). The underlying Si surface exhibits a structure similar to the H-terminated Si(100)1×3 surface (a), Eu atoms are adsorbed in pedestal and valley sites (b) in agreement with the STM features obtained at different biases (c). The bias voltages at which the different empty state STM features (labeled as A – E) were observed are indicated in (c). Four nonequivalent Si atoms with different bonding environments found within the suggested model, in agreement with the photoemission results [see Fig. 5.4.3(b)], are labeled as a, b, c, and f in (b). From Paper IV.*

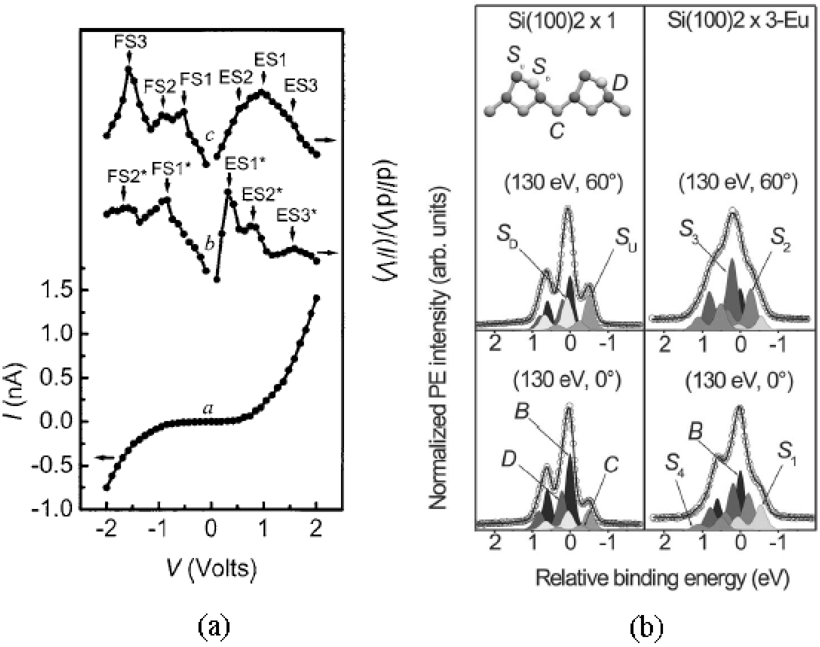

(a) (b)

Fig. 5.4.3. *Electronic structure measurements of clean Si(100) and Eu-Si(100)2×3 (a) Spectra obtained by STS: I-V spectrum of Eu-Si(100)2×3 (curve a), (dI/dV)/(I/V) spectra of Eu-Si(100)2×3 (curve b) and clean Si(100) (curve c). (b) Deconvolution of Si2p spectra measured by SR-PES using photon energy of 130 eV and emission angles 0° and 60°. Besides the bulk component B, four surface components are found for the clean Si(100)2×1 (S_U, S_D, D, and C) and for the Eu-Si(100)2×3 (S_1 – S_4). From Paper IV.*

On the vicinal Si(100), miscut by 4°, 2×3-type reconstructions similar to those described above, were verified in the low coverage (0.1 – 0.3 ML) regime [Paper II]. In addition, the adsorption of Eu and Yb drastically affects the step morphology. Adsorption of Eu almost preserves the terrace step configuration until at ~0.3 ML, when the terrace width is increased. In contrast, Yb induces a big modification to the terrace step configuration; single atomic layer steps appear which bunch into groups of several steps. As a result, terraces with either the 2×3 structure or perpendicular 3×2/4×2 structure occur. The photoemission results suggest that in the 2×3 and 3×2/4×2 phases the chemical environment and bonding configuration of the Si atoms are similar. Both RE metals tend to straighten the step edges, ie the number of kinks is less than on the clean surface.

In Paper III a double- to single-domain transition on the slightly miscut Eu/Si(100) surface at 0.4 ML was studied by LEED and STM. The smooth morphology of clean surface is broken, leading to the formation of an ordered domain pattern with lower 2×3 reconstructed terraces and higher “1×2” terraces composed of the so-called “wavy” structure, as shown in Fig. 5.4.4. The originally straight S_A steps convert into rough S_A’ steps, and rough S_B steps into straight S_B’ steps. The orientational phase transition is reversible: the reconstruction can be reverted to the double domain 2×3 phase by a partial desorption of Eu or to the double domain “1×2” reconstruction by extra adsorption. The origin of the phase transition is discussed in terms of an anisotropic strain in the 2×3 phase and a minimization of the length of domain boundaries, which is achieved when the boundaries are formed by the steps.

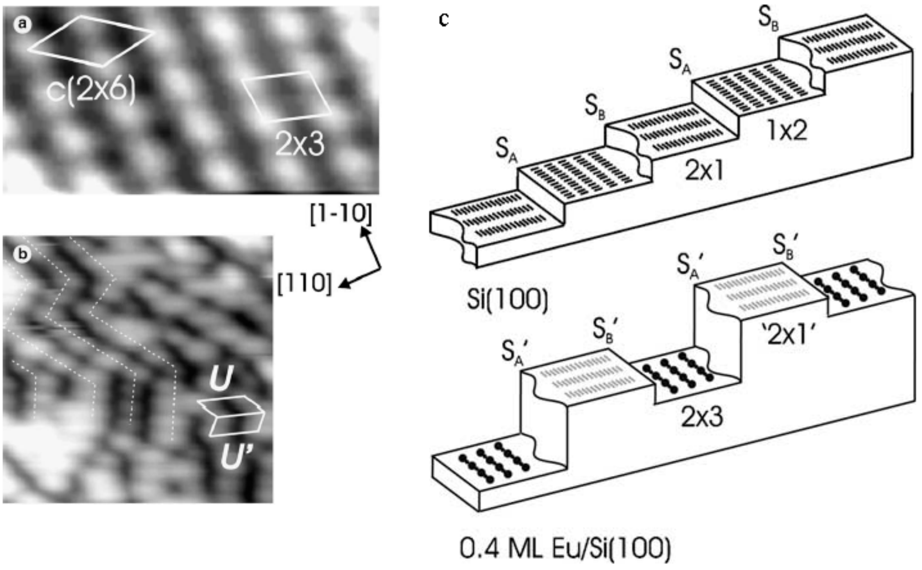

Fig. 5.4.4. *Empty-state STM images of the Eu/Si interface at 0.4 ML: (a) 2×3 and c(2×6) reconstructions and (b) “wavy” structure. In (c) schematic models of the clean Si(100) surface miscut by 0.4° (top) and the single domain Eu/Si surface at 0.4 ML of Eu (bottom) are shown. From Paper III.*

A similar wavy structure has been observed on Si(100)for Ba [185] and Sm [154]. All of these metals (Eu, Ba, and Sm) also exhibit the 2×3/c(2×6) phases. For Sm, the wavy structure was described as zig-zag defect chains surrounded by buckled Si dimers [154]. The model proposed for Ba consists of two oblique mirror symmetric unit cells containing buckled Ba dimers located on the second layer Si atoms, which have a dimerized 1×2 reconstruction [185]. The same kind of reconstruction can be adopted for Eu/Si based on the STM and LEED results; the (1×2) LEED pattern is suggested to originate from the underlying Si layer, as was suggested in the case of Ba/Si.

Papers V – VII

The formation of the Yb silicide phase was studied in Papers V – VII. On a flat Si(100) surface, the growth of the 3D silicide phase at 0.9 – 20 ML and the structure of the 2D wetting layer were studied by LEED and STM in Paper V, and silicide nanowire formation observed at 0.9 ML was studied by STM in Paper VI. In Paper VII, the Yb/Si interface formation was studied on a vicinal substrate by LEED and STM as a function of the coverage (1.0 – 4 ML) and the growth method.

The results from AES, TDS, and $\Delta\varphi$ measurements in Paper I revealed the onset of the Yb silicide phase formation occurring at a Yb coverage of 0.5 – 0.6 ML. The growth of Yb on Si(100) was found to follow the Stranski-Krastanov growth mechanism: a stable 2D wetting layer was observed to cover the surface prior to the 3D growth [Paper V, Paper VI]. This is in agreement with the TDS observation that the adsorbed 2D phases have a higher thermal stability than the 3D silicide phase, and therefore, the formation of the former is energetically more favourable than the formation of the latter.

The structure of 2D layer in the silicide growth regime is composed of rows, which can have different inter-row spacing leading to the specific 1×n periodicities. On the flat substrate 1×5, 1×9, and 1×3 periodicities were evidenced at low Yb coverage, whereas at high coverage and on the vicinal substrate, the 1×3 structure was found [Paper V, Paper VI].

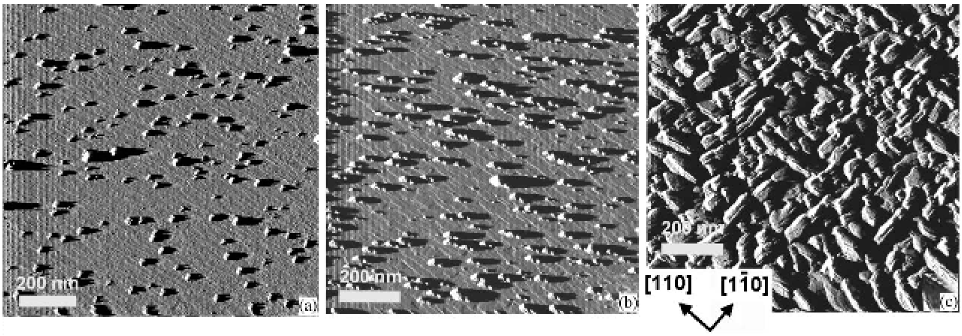

Fig. 5.4.5. *Evolution of the Yb/Si(100) surface morphology as a function of Yb coverage. Empty-state STM images at 0.9 ML (a), 2 ML (b), and 20 ML (c). From Paper V.*

Isolated 3D islands start to grow randomly on the 2D layer. The size and number of islands increase with the Yb coverage, as shown in Fig. 5.4.5. Almost complete coalescence is reached at 20 ML. Neither the hexagonal structure nor any long range ordering was found on top of the islands; however, the side faces of the 3D islands have a regular structure.

Despite earlier speculation that Yb would not form nanowires due to its relatively large lattice mismatch on both the hexagonal axis directions [149, 153], the growth of hexagonal AlB_2 type NWs was observed at 0.9 ML on the flat substrate [Paper VI]. Typical dimensions observed for such NWs were: height 0.3 – 1.0 nm, width ~ 6 nm, and length ~ 600 nm. It has been shown theoretically that an anisotropically strained island has always an anisotropic shape; it is thermodynamically favourable for the island to elongate only to one direction, which is the less-strained direction [186]. When applied to RE silicide nanowires, this implies that it is not necessary to have a large strain anisotropy; a small difference in the lattice mismatch in the two directions may be sufficient to promote the growth along one direction. In contrast to other RE/Si(100) nanowire systems, an unexpectedly wide variety of wire orientations was observed, namely, [011], $[0\bar{1}1]$, and [001]. The wire grown along the [001] direction, ie, the off-*a*-axis direction, reveals a lattice structure where the silicide *a*- and *c*-axes are still parallel to the $[0\bar{1}1]$ Si directions but not the longer and shorter axes of nanowires. This is believed to be a consequence of the somewhat enhanced (in terms of the other RE silicides) mismatch along the $[11\bar{2}0]$ azimuth for the hexagonal Yb silicide (-1.6 %).

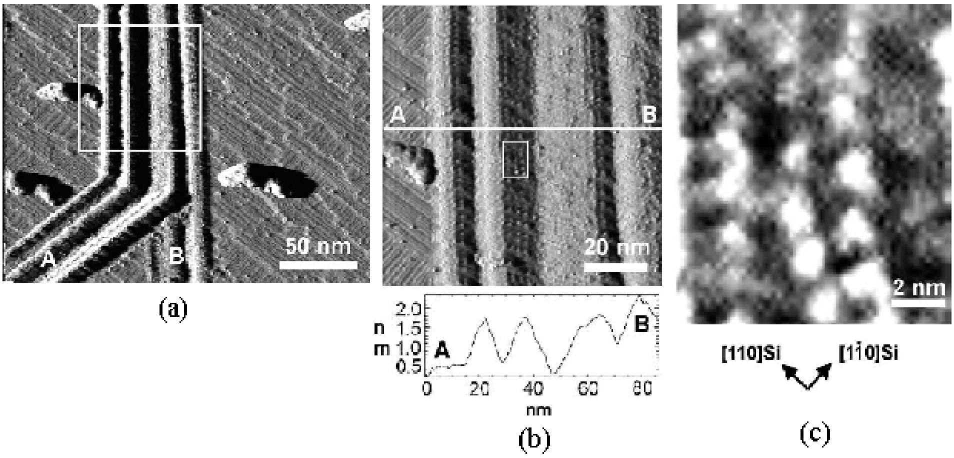

Fig. 5.4.6. *(a) Collision of two Yb silicide nanowires, labeled as A and B, on a flat Si(100) surface oriented in the $[0\bar{1}1]$ and [001] directions, respectively. (b) Magnification of the boxed area in (a) and a line profile across the NW bundle. (c) Magnification of the side face of the NW highlighted by a box in (b). From Paper VI.*

On the vicinal Si(100) substrate miscut by 4°, the formation of nanowires vs. 3D island growth, as well as the orientation of the Yb-induced 2D reconstruction, showed dependence on the growth method [Paper VII]. Ytterbium was either deposited at RT followed by annealing at ~ 610 °C, or the deposition was performed directly onto the surface at an elevated temperature of ~ 610 °C.

Figure 5.4.7. shows the 2D wetting layer reconstruction, which in STM images appears as a stripelike structure. The spacing between individual stripes is 3*a*, which induces the 3× periodicity seen in the corresponding LEED patterns. Deposition at RT, followed by annealing at ~ 610 °C, produced the stripes oriented perpendicular to the step edges [Fig. 5.4.6 (a)] whereas deposition at ~ 610 °C produced stripes running parallel to the step edges [Fig. 5.4.7 (b)].

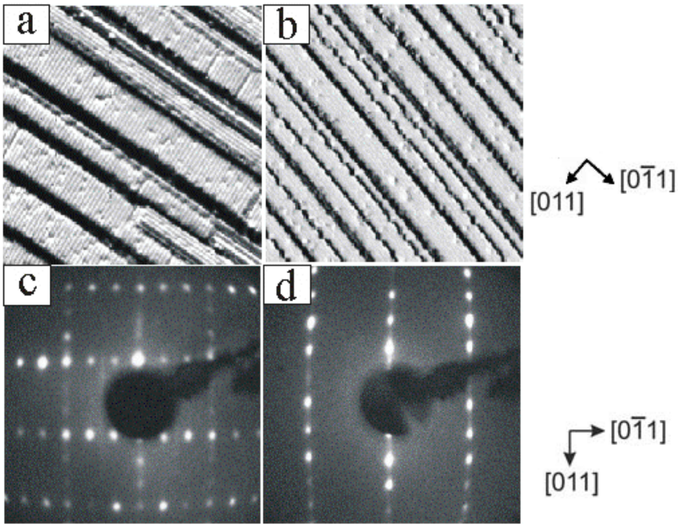

Fig. 5.4.7. *Empty-state STM images of Yb-induced 2D reconstructions on vicinal Si(100) and corresponding LEED patterns. (a) and (c) 2.0 ML Yb deposited at RT and subsequently annealed at ~ 610 °C, (b) and (d) 4.0 ML Yb deposited at ~ 610 °C. The switchover of stripe orientation is evidenced. From Paper VII.*

The Yb deposition at RT followed by annealing induces a 3D phase formation similar to the flat Yb/Si(100) system; small islands start to grow randomly on the top of the 2D layer and the number and size of islands increases with increasing coverage. Figure 5.4.8 (a) shows the islands on the surface, which has 2.5 ML of Yb deposited at RT and is subsequently annealed at 610 °C. The height of the islands is typically a few nanometers, and their diameters vary in the range of 5 to 50 nm.

The growth of NWs was observed on the samples deposited directly at 610 ºC. At 2.5 ML, pseudo-nanowires appeared as compact rods with their longer side oriented along the steps. The rod in Fig. 5.4.8 (b) has width and height about 19 and 4 nm, respectively, and its sides have a stepped structure resembling the 3D island sides in (a), suggesting the epitaxial quality of the 3D rod bulk structure. The top of the rod is atomically smooth, and its atomic structure was revealed to be composed of (3×2) building blocks. When Yb coverage is increased to about 4 ML, the NWs appear as bundles of two or more wires. Typically their length is hundreds of nanometers, but some of them extend to thousands of nanometers, as in Fig. 5.4.8 (c). The width of the

NWs is 10 – 40 nm and height 4 – 6 nm for the wires in the length range of hundreds of nanometers. For the longer wires, the width and height are larger. The detailed atomic structure of the NWs remains unsolved. However, ordered dislocations running in two directions, across and along the wires, were found. In particular, a periodicity of 9*a* along the NW was observed, in good agreement with the (3×2) structure found for the rod. Such periodicities are also consistent with the hexagonal AlB_2 structure. Under the growth conditions used in this study, the Si rich silicide phase is expected to form [132]. Taking into account the phase diagrams of the Yb-Si system [187, 188] and the fact that a lattice mismatch of up to ~ 2 % can be compensated by the elastic strain [189], the only plausible silicide phase with appropriate lattice parameters for 1D growth is the hexagonal $YbSi_{2-x}$ structure.

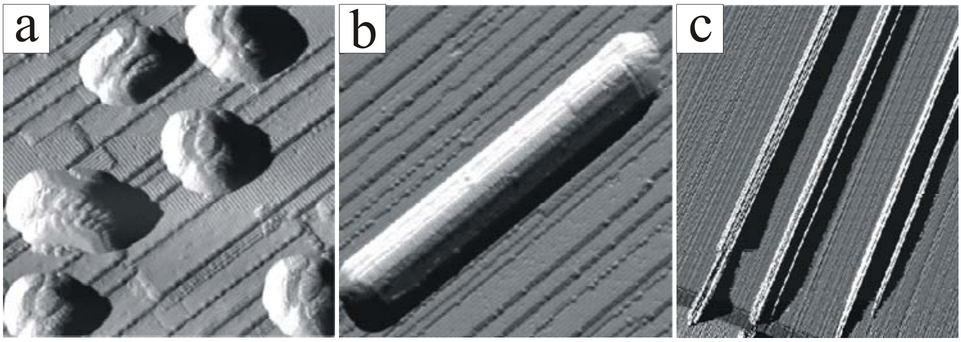

Fig. 5.4.8. *STM images of 3D growth on the vicinal Yb/Si(100) interface. (a) Islands induced by deposition of 2.5 ML Yb at RT and subsequent annealing at 610 ºC, 100×100 nm^2. Nanowires are formed due to deposition of 4 ML Yb at 610 ºC: (b) a compact rod, 85×85 nm^2, (c) bundles of nanowires, 1510×2000 nm^2. From Paper VII.*

The formation of the 2D reconstructions and the silicide phase requires the rearrangement and mass transport of both Si and Yb atoms. When the two Yb-induced 2D structures with orthogonal (3×1) and (1×3) units are formed on the single-domain Si(100)2×1 surface, the upper-most Si layer is expected to be removed in order to provide the rotation of the (3×1)-type domain by 90°. Such Si rearrangement can play an important role in the process of the Yb silicide formation and may drive the 1D Yb silicide growth. The Yb silicide NWs are found only upon Yb deposition at the elevated temperature, that is, with the (1×3) arrangement of the 2D layer. On this basis, it can be assumed that the formation of the unidirectional (1×3) reconstruction stimulates the 1D silicide growth in the Yb/Si(100) system. It still remains unclear whether or not the substrate temperature critically affects the Yb silicide growth.

6. Summary

In this thesis, the formation of the RE/Si(100) interface (RE = Eu, Yb) has been studied using several experimental methods, mainly LEED, STM/STS, and photoemission. The substrates were either nominally flat or vicinal Si(100) surfaces. The two stages which can be distinguished in the process, namely the formation of an adsorbed 2D layer and a growth 3D silicide phase, were examined in detail.

It was demonstrated that Eu and Yb induce a rich variety of 2D reconstructions. Atomic models were proposed for the 2×3 type structure observed for both metals. Even though such structures appear geometrically similar and the electronic configurations of Eu and Yb are closely related, no common model was found. The 2×3 unit cell contains two metal atoms, which for Yb are on valley sites of the unreconstructed 1×1 surface, whereas for Eu the formation of the 2×3 unit cell includes rearrangement of the underlying Si atoms into a structure similar to the H-terminated Si(100) 1×3 surface. Therefore, the adsorbate atoms have a significant role in the formation of 2×3-type structures on Si(100). To further understand the structure of the (2×3) and (2×4) phases, theoretical calculations are required. Recently, first-principles *ab initio* DFT calculations were performed for Yb/Si(100)-(2×3) and -(2×4) structures [Paper XVII] and a similar work is under process for the Eu/Si(100)-(2×3) system.

The morphology and orientational symmetry of the Si(100) surface are affected by Eu and Yb adsorption. For Eu, a reversible double- to single-domain transition was observed at 0.4 ML on a slightly miscut substrate. The structure was formed by alternating lower 2×3 reconstructed terraces and higher “1×2” terraces composed of the so-called “wavy” structure. The step edge configuration was also altered; initially straight step edges were converted to rough ones and vice versa. For vicinal substrates, the adsorbates induced a remarkable straightening of step edges. The surface configuration with terraces separated by equally spaced steps was disrupted due to RE metal adsorption; the terrace width and step height varied depending on the adsorbate atom and coverage. The growth method as well as Yb coverage had a significant effect in the orientation of the Yb-induced 3×1-type 2D wetting layer reconstruction on a vicinal substrate. The deposition of Yb at RT, followed by subsequent annealing at ~ 610 °C, lead to an orientation perpendicular to the step edges, whereas a deposition directly at 610 °C produced the reconstruction with orientation parallel to the step edges. At low coverages, stripes running across and along the step edges coexisted.

The onset of the Yb silicide phase formation occurred at 0.5 – 0.6 ML and growth proceeded via the Stranski-Krastanov mode. On the flat substrate, the growth of the silicide phase as 3D islands was observed up to a coverage of 20 ML, at which point an almost complete coalescence of islands was seen.

The growth on Yb silicide nanowires with the hexagonal AlB_2-type structure, which has an anisotropic lattice mismatch with the Si(100) surface, was demonstrated. The nanowires were observed on a flat substrate at 0.9 ML exhibiting unexpectedly large variety of growth directions.

On a vicinal substrate, the form of the Yb silicide phase was shown to be strongly dependent on the growth conditions. When deposited at RT and subsequently annealed, Yb induced a 3D silicide island growth similar to that observed on a flat substrate.

Deposition directly at 610 °C lead to the formation of NWs oriented parallel to the step edges.

References

[1] *Handbook of Surface Science, Vol. 1, Physical structure*, W. N. Unertl, Ed., Elsevier Science B. V., Netherlands (1996).
[2] R. E. Schlier and H. E. Farnsworth, J. Chem. Phys. 30, 917 (1959).
[3] J. J. Lander and J. Morrison, J. Chem. Phys. 37, 729 (1962).
[4] T. D. Poppendieck, T. C. Ngoc and M. B. Webb, Surf. Sci. 75, 287 (1978).
[5] M. J. Cardillo and G. E. Becker, Phys. Rev. B 21, 1497 (1980).
[6] R. Seiwatz, Surf. Sci. 2, 473 (1964).
[7] F. Jona, H. D. Shih, A. Ignatiev, D. W. Jepson and P. M. Marcus, J. Phys. C 10, L67 (1977).
[8] D. J. Chadi, Phys. Rev. Lett. 43, 43 (1979).
[9] D. J. Chadi, J. Vac. Sci. Technol. 16, 1290 (1979).
[10] J. E. Northrup, Phys. Rev. Lett. 54, 815 (1985).
[11] R. M. Tromp, R. J. Hamers and J. E. Demuth, Phys. Rev. Lett. 55, 1303 (1985).
[12] R. J. Hamers, R. M. Tromp and J. E. Demuth, Phys. Rev. B 34, 5343 (1986).
[13] J. E. Rowe and H. Ibach, Phys. Rev. Lett. 32, 421 (1974).
[14] F. J. Himpsel and D. E. Eastman, J. Vac. Sci. Technol. 16, 1297 (1979).
[15] R. I. G. Uhrberg, G. V. Hansson, J. M. Nicholls and S. A. Flodström, Phys. Rev. B 24, 4684 (1981).
[16] J. P. LaFemina, Surf. Sci. Rep. 16, 137 (1992).
[17] J. Ihm, M. L. Cohen, D. J. Chadi, Phys. Rev. B 21, 4592 (1980).
[18] M. T. Yin, M. L. Cohen, Phys. Rev. B 24, 2303 (1981).
[19] W. S. Verwoerd, Surf. Sci. 99, 581 (1980).
[20] W. S. Verwoerd, Surf. Sci. 129, 419 (1983).
[21] M. A. Bowen, J. D. Dow, R. E. Allen, Phys. Rev. B 26, 7083 (1982).
[22] J. Ihm, D. H. Lee, J. D. Joannopoulos, J. J. Xiong, Phys. Rev. Lett. 51, 1872 (1983).
[23] A.Mazur, J. Pollmann, Phys. Rev. B 26, 7086 (1982).
[24] P. Krüger, A. Mazur, J. Pollmann,G. Wolfgarten, Phys. Rev. Lett. 57, 1468 (1986).
[25] O. L. Alerhard and E. J. Mele, Phys. Rev. B 35, 5533 (1987).
[26] T. Tabata, T. Aruga, Y. Murata, Surf. Sci. 179, L63 (1987).
[27] Z. Shu, N. Shima, M. Tsukada, Phys. Rev. B 40, 11868 (1989).
[28] N. Roberts, R. J. Needs, Surf. Sci. 236, 112 (1990).
[29] J. H. Wilson, J. D. Todd, A. P. Sutton, J. Phys. Condens. Matter 2, 10259 (1990).
[30] K. Kobayashi, Y. Morikawa, K. Terakura, S. Blügel, Phys. Rev. B 45, 3469 (1992).
[31] J. Dabrowski, M. Scheffler, Appl. Surf. Sci. 56-58, 15 (1992).
[32] A. I. Shkrebtii, R. Del Sole, Phys. Rev. Lett. 70, 2645 (1993).
[33] A. Ramstad, G. Brocks, P. J. Kelly, Phys. Rev. B 51, 14504 (1995).
[34] P. Krüger, J. Pollmann, Phys. Rev. B 38, 10578 (1988).
[35] P. Krüger, J. Pollmann, Phys. Rev. Lett. 74, 1155 (1995).
[36] R. Gunnella, E. L. Bullock, L. Patthey, C. R. Natoli, T. Abukawa, S. Kono, L. S. O. Johansson, Phys. Rev. B 57, 14739 (1998).
[37] E. Artacho, F. Yndurain, Phys. Rev. Lett. 62, 2491 (1989).
[38] I. P. Batra, Phys. Rev. B 41, 5048 (1990).
[39] F. J. Himpsel, P. Heimann, T.-C. Chiang and D. E. Eastman, Phys. Rev. Lett. 45, 1112 (1980).
[40] W. Mönch, P. Koke, S. Krueger, J. Vac. Sci. Technol. 19, 313 (1981).
[41] B. W. Holland, C. B. Duke, A. Paton, Surf. Sci. 140, L269 (1984).
[42] Y. Enta, S. Suzuki, S. Kono, Phys. Rev. Lett. 65, 2704 (1990).
[43] L. S. O. Johansson, B. Reihl, Surf. Sci. 269/270, 810 (1992).
[44] R. A. Wolkov, Phys. Rev. Lett. 68, 2636 (1992).

[45] E. Landemark, C. J. Karlsson, Y.-C. Chao, R. I. G. Uhrberg, Phys. Rev. Lett. 69, 1588 (1992).
[46] E. Fontes, J. R: Patel, F. Comin, Phys. Rev. Lett. 70, 2790 (1993).
[47] H. Tochihara, T. Amakusa, M. Iwatsuki, Phys. Rev. B 50, 12262 (1994).
[48] A.W. Munz, C. Ziegler and W. Göpel, Surf. Sci. 325, 177 (1995).
[49] E. L. Bullock, R. Gunnella, L. Patthey, T. Abukawa, S. Kono, C. R. Natoli, L. S. O. Johansson, Phys. Rev. Lett. 74, 2244 (1995).
[50] A.I. Shkrebtii, R. Di Felice, C. M. Bertoni, R. Del Sole, Phys. Rev. B 51, 11201 (1995).
[51] M. Ono, A. Kamoshida, N. Matsuura, E. Ishikawa, T Eguchi and Y. Hasegawa, Phys. Rev. B 67, 201306(R)(2003).
[52] *Handbook of Surface Science, Vol. 2, Electronic structure*, K. Horn and M. Scheffler, Ed., Elsevier Science B. V., Netherlands (2000).
[53] D. J. Chadi, Phys. Rev. Lett. 59, 1691 (1987).
[54] T. W. Poon, S. Yip, P. S. Ho, F. F. Abraham, Phys. Rev. B 45, 3521 (1992).
[55] P. Boguslawski, Q.-M. Zhang, Z. Zhang, J. Bernholc, Phys. Rev. Lett. 72, 3694 (1994).
[56] A. Oshiyama, Phys. Rev. Lett. 74, 130 (1995).
[57] B. S. Swartzentruber, Y.-W. Mo, R. Kariotis, M. G. Lagally, M. B. Webb, Phys. Rev. Lett. 65, 1913 (1990).
[58] D. J. Eaglesham, A. E. White, L. C. Feldman, N. Moriya, D. C. Jacobson, Phys. Rev. Lett. 70, 1643 (1993).
[59] H. J. W. Zandvliet, S. van Dijken, B. Poelsema, Phys. Rev. B 53, 15429 (1996).
[60] O. L. Alerhand, D. Vanderbilt, R. D. Meade, J. D. Joannopoulos, Phys. Rev. Lett. 61, 1973 (1988).
[61] R. M. Tromp, M. C. Reuter, Phys. Rev. B 47, 7598 (1993).
[62] R. M. Tromp, M. C. Reuter, Phys. Rev. Lett. 68, 820 (1992).
[63] P. E. Wierenga, J. A. Kubby and J. E. Griffith, Phys. Rev. Lett. 59, 2169 (1987).
[64] O. L. Alerhand, A. N. Berker, J. D. Joannopoulos, D. Vanderbilt, R. J. Hamers and J. E. Demuth, Phys. Rev. Lett. 64, 2406 (1990).
[65] X. Tong and P. A. Bennett, Phys. Rev. Lett. 67, 101 (1991).
[66] B. S. Swartzentruber, N. Kitamura, M. G. Lagally and M. B. Webb, Phys. Rev. B 47, 13432 (1993).
[67] E. Pehlke, J. Tersoff, Phys. Rev. Lett. 67, 465 (1991).
[68] E. Pehlke, J. Tersoff, Phys. Rev. Lett. 67, 1290 (1991).
[69] T. Yokoyama, K. Takayanagi, Phys. Rev. B 57, R4226 (1998).
[70] K. Yagi, H. Minoda and M. Degawa, Surf. Sci. Rep. 43, 45 (2001).
[71] A. V. Latyshev, L. V. Litvin and A. L. Aseev, Appl. Surf. Sci. 130-132, 139 (1998).
[72] H. Minoda, T. Shimakura, K. Yagi, F.-J. Meyer zu Heringdorf and M. Horn von Hoegen, Phys. Rev. B 61, 5672 (2000).
[73] S. Fölsch, G. Meyer, K. H. Rieder, M. Horn von Hoegen, T. Schmidt and M. Henzler, Surf. Sci. 394, 60 (1997).
[74] H. J. W. Zandvliet, Rev. Mod. Phys. 72, 593 (2000).
[75] H.-C. Jeong, E. D. Williams, Surf. Sci. Rep. 34, 171 (1999).
[76] H. J. W. Zandvliet, H. B. Elswijk, E. J. van Loenen, D. Dijkkamp, Phys. Rev. B 45, 5965 (1992).
[77] E. E. Gruber, W. W. Mullins, J. Phys. Chem. Solids 28, 875 (1967).
[78] H. J. W. Zandvliet, H. B. Elswijk, Phys. Rev. B 48, 14269 (1993).
[79] R. J. Hamers, U. K. Kohler, J. Vac. Sci. Technol. A7, 2854 (1990).
[80] J. Wang, T. A. Arias, J. D. Joannopoulos, Phys. Rev. B 47, 10497 (1993).
[81] M. Z. Hossain, Y. Yamashita, K. Mukai, J. Yoshinobu, Phys. Rev. B 67, 153307 (2003).
[82] S. Okano, A. Oshiyama, Surf. Sci. 554, 272 (2004).

[83] J.-Y. Koo, J.-Y. Yi, C. Hwang, D.-H. Kim, S. Lee, D.-H. Shin, Phys. Rev. B 52, 17269 (1995).

[84] H. Niehus, U. K. Kohler, M. Copel, J. E. Demuth, J. Microscopy 152, 735 (1988).

[85] H. J. W. Zandvliet, H. K. Louwsma, P. E. Hegeman, B. Poelsema, Phys. Rev. Lett. 75, 3890 (1995).

[86] J. Tersoff, Phys. Rev. B 45, 8833 (1992).

[87] J. Oviedo, D. R. Bowler, M. J. Gillan, Surf. Sci. 515, 483 (2002).

[88] C. Davisson, L. H. Germer; Phys. Rev. 30, 705 (1927).

[89] *Surface Analysis – The Principal Techniques*, J. C. Vickerman, Ed., John Wiley & Sons, West Sussex (1997).

[90] G. Ertl and J. Küppers, *Low Energy Electrons and Surface Chemistry – 2nd, completely rev. ed.*, VCH Verlagsgesellschaft mbH, Weinheim (1985).

[91] U. Scheithauer, G. Meyer, M. Henzler, Surf. Sci. 178, 441 (1986).

[92] J. B. Pendry, *Low Energy Electron Diffraction*, Academic Press, New York (1974).

[93] M. Van Hove, W. H. Weinberg, C.-M. Chan, *Low Energy Electron Diffraction*, Springer Series in Surface Science, Vol. 6. Springer, Berlin, Heidelberg (1986).

[94] G. Binnig, H. Rohrer, Ch. Gerber and E. Weibel, Phys. Rev. Lett. 49, 57 (1982).

[95] G. Binnig, H. Rohrer, Ch. Gerber and E. Weibel, Appl. Phys. Lett. 40, 178 (1982).

[96] G. Binnig, H. Rohrer, Ch. Gerber and E. Weibel, Phys. Rev. Lett. 50, 120 (1983).

[97] J. Tersoff, D. R. Hamann, Phys. Rev. B 31, 805 (1985).

[98] N. D. Lang, Phys. Rev. Lett. 55, 230 (1985).

[99] M. Tsukada, K. Kobayashi, N. Isshiki and H. Kageshima, Surf. Sci. Rep. 13, 265 (1991).

[100] J. Bardeen, Phys. Rev. Lett. 6, 57 (1961).

[101] J. A. Kubby and J. J. Boland, Surf. Sci. Rep. 26, 61 (1996).

[102] R. J. Hamers, Annu. Rev. Phys. Chem. 40, 531 (1989).

[103] R. J. Hamers, R. M. Tromp and J. E. Demuth, Phys. Rev. Lett. 56, 1972 (1986).

[104] R. M. Feenstra, J. A. Stroscio and A. P. Fein, Surf. Sci. 181, 295 (1987).

[105] K.-H. Rieder *et al.*, J. Phys.: Conf. Ser. 19, 175 (2005).

[106] D. M. Eigler and E. K. Schweizer, Nature 344, 524 (1990).

[107] S.-W. Hla, J. Vac. Sci. Tech. B 23, 1351 (2005).

[108] S.-W. Hla, L. Bartels, G. Meyer and K.-H. Rieder, Phys. Rev. Lett. 85, 2777 (2000).

[109] G. Margaritondo, *Introduction to Synchrotron Radiation*, Oxford University Press, New York (1988).

[110] D. Attwood, *Soft X-rays and Extreme Ultraviolet Radiation: Principles and Applications*, Cambridge University Press (1999).

[111] M. Terasawa, M. Kihara, Analytical Spectroscopy Library 7, 1 (1996).

[112] C. N. Berglund and W. E. Spicer, Phys. Rev. 136, A1030 (1964).

[113] C. N. Berglund and W. E. Spicer, Phys. Rev. 136, A1044 (1964).

[114] S. Hüfner, *Photoelectron Spectroscopy: Principles and Applications*, Springer-Verlag, Berlin (1995).

[115] D. Briggs and M.P. Seah, *Practical Surface Analysis, Vol. 1: Auger and X-ray Photoelectron Spectroscopy*, John Wiley & Sons, West Sussex (1990).

[116] W. F. Egelhoff, Surf. Sci. Rep. 6, 253 (1986).

[117] *Topics in applied Physics, Vol. 26, Photoemission in Solids I. General Principles*, M. Gordona and L. Ley, Ed., Springer-Verlag, Berlin (1978).

[118] P. H. Citrin, G. K. Wertheim and Y. Baer, Phys. Rev. Lett. 41, 1425 (1978).

[119] A. R. Williams, N. D. Lang, Phys. Rev. Lett. 40, 954 (1978).

[120] D. Spanjaard, C. Guillot, M.-C. Desjonquères, G. Tréglia and J. Lecante, Surf. Sci. Rep. 5, 1 (1985).

[121] B. Johansson, N. Mårtensson, Phys. Rev. B 21, 4427 (1980).

[122] E. Pehlke, M. Scheffler, Phys. Rev. Lett. 71, 2338 (1993).

[123] D. A. Shirley, Phys. Rev. B 5, 4709 (1971).

[124] A. M. de Jong, J. W. Niemantsverdriet, Surf. Sci. 233, 355 (1990).

[125] N. W. Ashcroft and N. D. Mermin, *Solid State Physics*, W. B. Saunders Company, Philadelphia (1976).

[126] T. Ollonqvist, Doctoral Thesis, *Vacuum ultraviolet grating inverse photoemission spectrometer: Instrumentation and applications*, University of Turku Publications 269, Turku (2001).

[127] http://maxsun5.maxlab.lu.se/beamlines/bl33/

[128] T. V. Krachino, M. V. Kuzmin, M. V. Loginov and M. A. Mittsev, Phys. Solid State 39, 224 (1997).

[129] T. V. Krachino, M. V. Kuzmin, M. V. Loginov and M. A. Mittsev, Phys. Low Dim. Struct. 9/10, 95 (1999).

[130] R. D. Thompson, K. N. Tu, Thin Solid Films 93, 265 (1982).

[131] G. Rossi, Surf. Sci. Rep. 7, 1 (1987).

[132] F. P. Netzer, J. Phys.: Condens. Matter 7, 991 (1995).

[133] J. A. Knapp, S. T. Picraux, Appl. Phys. Lett. 48, 466 (1986).

[134] P. Paki, U. Kafader, P. Wetzel, C. Pirri, J. C. Peruchetti, D. Bolmont, G. Gewinner, Phys. Rev. B 45, 8490 (1992).

[135] B. Johansson, Phys. Rev. B 20, 1315 (1979).

[136] W. A. Henle, M. G. Ramsey, F. P. Netzer, Surf. Sci. 254, 182 (1991).

[137] R. Hofmann, W. A. Henle, F. P. Netzer, M. Neuber, Phys. Rev. B 46, 3857 (1992).

[138] W. A. Henle, F. P. Netzer, R. Cimino, W. Braun, Surf. Sci. 221, 131 (1989).

[139] V. M. Koleshko, V. F. Belitsky, A. A. Khodin, Thin Solid Films 141, 277 (1986).

[140] J. Onsgaard, J. Ghijsen, R. L. Johnson, F. Ørskov, I. Chorkendorff, F. Grey, J. Electron Spectrosc. Relat. Phenom. 52, 67 (1990).

[141] P. J. Godowski, J. Onsgaard, F. Ørskov, M. Christiansen, J. Mater. Sci. Lett. 9, 989 (1990).

[142] J. Onsgaard, M. Christiansen, F. Ørskov, P. J. Godowski, Surf. Sci. 247, 208 (1991).

[143] W. A. Henle, M. G. Ramsey, F. P. Netzer, S. Witzel, W. Braun, Surf. Sci. 243, 141 (1991).

[144] A. Travlos, P. Aloupogiannis, E. Rokofyllou, C. Papastaïkoudis, G. Weber, A. Traverse, J. Appl. Phys. 72, 948 (1992).

[145] Y. K. Lee, N. Fujimura, T. Ito, N. Itoh, J. Cryst. Growth 134, 247 (1993).

[146] Y. K. Lee, N. Fujimura, T. Ito, J. Alloys and Compounds 193, 289 (1993).

[147] C. Preinesberger, S. Vandré, T. Kalka, M. Dähne-Prietsch, J. Phys. D: Appl. Phys. 31, L43 (1998).

[148] Y. Chen, D. A. A. Ohlberg, G. Medeiros-Ribeiro, Y. A. Chang, R. S. Williams, Appl. Phys. Lett. 76, 4004 (2000).

[149] J. Nogami, B. Z. Liu, M. V. Katkov, C. Ohbuchi, N. O. Birge, Phys. Rev. B 63, 233305 (2001).

[150] C. Ohbuchi, J. Nogami, Phys. Rev. B 66, 165323 (2002).

[151] J. H. G. Owen, K. Miki, D. R. Bowler, J. Mater. Sci. 41, 4568 (2006).

[152] R. Ragan, S. Kim, X. Li, R. S. Williams, Appl. Phys. A 80, 1339 (2005).

[153] M. V. Katkov, J. Nogami, Surf. Sci. 524, 129 (2003).

[154] C. Ohbuchi, J. Nogami, Surf. Sci. 579, 157 (2005).

[155] J. Yang, Q. Cai, X.-D. Wang, R. Koch, Surf. Sci. 526, 291 (2003).

[156] B. Z. Liu, J. Nogami, Surf. Sci. 540, 136 (2003).

[157] B. C. Harrison, P. Ryan, J. J. Boland, Surf. Sci. 582, 79 (2005).

[158] B. Z. Liu, J. Nogami, Surf. Sci. 488, 399 (2001).

[159] B. Z. Liu, J. Nogami, J. Appl. Phys. 93, 593 (2003).

[160] Q. Cai, J. Yang, Y. Fu, Y. Wang, X. Wang, Appl. Surf. Sci. 190, 157 (2002).

[161] T. Kalka, C. Preinesberger, S. Vandré, M. Dähne-Prietsch, Appl. Phys. A 66, S1073 (1998).
[162] C. Preinesberger, S. K. Becker, S. Vandré, T. Kalka, M. Dähne, J. Appl. Phys. 91, 1695 (2002).
[163] K. S. Chi, W. C. Tsai, L. J. Chen, J. Appl. Phys. 93, 153 (2003).
[164] A. Travlos, N. Salamouras, N. Boukos, J. Phys. Chem. Solids 64, 87 (2003).
[165] C. H. Luo, L. J. Chen, J. Appl. Phys. 82, 3808 (1997).
[166] L. Magaud, A. Pasturel, G. Kresse, J. Hafner, Phys. Rev. B 55, 13479 (1997).
[167] C.-X. Ji, M. Huang, J.-H. Yang, Y. A. Chang, R. Ragan, Y. Chen, D. A. A. Ohlberg, R. S. Williams, Appl. Phys. A 78, 287 (2004).
[168] Y. Chen, D. A. A. Ohlberg, R. S. Williams, Mater. Sci. Eng. B 87, 224 (2001).
[169] Y. Chen, D. A. A. Ohlberg, G. Medeiros-Ribeiro, Y. A. Chang, R. S. Williams, Appl. Phys. A 75, 353 (2002).
[170] G. Chen, J. Wan, J. Yang, X. Ding, L. Ye, X. Wang, Surf. Sci. 513, 203 (2002).
[171] Y.-K. Lee, M.-S. Lee, J.-S. Lee, J. Cryst. Growth 244, 305 (2002).
[172] Q. Cai, W. Zhou, J. Phys. Condens. Matter 16, 6835 (2004).
[173] J. Yang, Q. Cai, X.-D. Wang, R. Koch, Surf. Interface Anal. 36, 104 (2004).
[174] S. Harako, K. Kouno, S. Komuro, A. Ohata, X. Zhao, J. Cryst. Growth 275, e2263 (2005).
[175] W. C. Tsai, H. C. Hsu, H. F. Hsu, L. J. Chen, Appl. Surf. Sci. 244, 115 (2005).
[176] W. Zhou, Y. Zhu, T. Ji, X. Hou, Q. Cai, Nanotech. 17, 852 (2006).
[177] Y. Chen, D. A. A. Ohlberg, R. S. Williams, J. Appl. Phys. 91, 3213 (2002).
[178] R. Ragan, Y. Chen, D. A. A. Ohlberg, G. Medeiros-Ribeiro, R. S. Williams, J. Cryst. Growth 251, 657 (2003).
[179] D. Lee, D. K. Lim, S. S. Bae, S. Kim, R. Ragan, D. A. A. Ohlberg, Y. Chen, R. S. Williams, Appl. Phys. A 80, 1311 (2005).
[180] Z. He, D. J. Smith, P. A. Bennett, Phys. Rev. B 70, 241402(R) (2004).
[181] B. Z. Liu, J. Nogami, Nanotech. 14, 873 (2003).
[182] D. Lee, S. Kim, Appl. Phys. Lett. 82, 2619 (2003).
[183] B. C. Harrison, J. J. Boland, Surf. Sci. 594, 93 (2005).
[184] H. Lee, D. Lee, D. K. Lim, S. Kim, C. Hwang, Surf. Sci. 600, 1283 (2006).
[185] K. Ojima, M. Yoshimura, K. Ueda, Phys. Rev. B 65, 075408 (2002).
[186] A. Pradham, N.-Y. Ma, F. Liu, Phys. Rev. B 70, 193405 (2004).
[187] A. Palenzona, P. Manfrinetti, S. Brutti, G. Balducci, J. Alloys Comp. 348, 100 (2003).
[188] S. Brutti, G. Balducci, A. Ciccioli, G. Gigli, Computer Coupling of Phase Diagrams and Thermochemistry 29, 254 (2005).
[189] A. M. Andrews, J. S. Speck, J. Appl. Phys. 91, 1933 (2002).